

Modelling Grain Rotational Disruption by Radiative Torques and Extinction of Active Galactic Nuclei

NGUYEN CHAU GIANG,^{1,2,3} THIEM HOANG,^{1,2}

¹*Korea Astronomy and Space Science Institute, Daejeon 34055, Republic of Korea; thiemhoang@kasi.re.kr*

²*Korea University of Science and Technology, Daejeon 34113, Republic of Korea*

³*University of Science and Technology of Hanoi, VAST, 18 Hoang Quoc Viet, Vietnam*

ABSTRACT

Extinction curves observed toward individual Active Galactic Nuclei (AGN) usually show a steep rise toward far-ultraviolet (FUV) wavelengths and can be described by the Small Magellanic Cloud (SMC)-like dust model. This feature suggests the dominance of small dust grains of size $a \leq 0.1 \mu\text{m}$ in the local environment of AGN, but the origin of such small grains is unclear. In this paper, we aim to explain this observed feature by applying the Radiative Torque Disruption (RATD) to model the extinction of AGN radiation from FUV to mid-infrared (MIR) wavelengths. We find that in the intense radiation field of AGN, large composite grains of size $a \geq 0.1 \mu\text{m}$ are significantly disrupted to smaller sizes by RATD up to $d_{\text{RATD}} > 100 \text{ pc}$ in the polar direction and $d_{\text{RATD}} \sim 10 \text{ pc}$ in the torus region. Consequently, optical-MIR extinction decreases, whereas FUV-near-ultraviolet (NUV) extinction increases, producing a steep far-UV rise extinction curve. The resulting total-to-selective visual extinction ratio thus significantly drops to $R_V < 3.1$ with decreasing distances to AGN center due to the enhancement of small grains. The dependence of R_V with the efficiency of RATD will help us to study the dust properties in the AGN environment via photometric observations. In addition, we suggest that the combination of the strength between RATD and other dust destruction mechanisms which are responsible for destroying very small grains of $a \leq 0.05 \mu\text{m}$ is the key for explaining the dichotomy observed 'SMC' and 'gray' extinction curve toward many AGN.

Keywords: active galactic nuclei: dust, extinction

1. INTRODUCTION

The unified model (Antonucci 1993, Urry & Padovani 1995) of Active Galactic Nuclei (AGN) posits that all radio-quiet AGN are intrinsically the same, and the difference in their observational properties arises from the inclination effects due to the presence of an optically thick dusty torus around the nuclei. When observing AGN from an inclined angle (i.e., not perpendicular to the disk), the ultraviolet (UV)-optical radiation from the accretion disk and the line emission from the broad-line region (BLR) are absorbed by the dusty torus. Thus, the UV-optical signal from these regions is absent in the observed spectrum of AGN (i.e., type 2 AGN). In contrast, when looking AGN in the perpendicular direction to the disk (face-on), the UV-optical radiation emitting from the central region is not significantly attenuated due to the small presence of dust grains along the polar direction (i.e., type 1 AGN).

The absorption of UV-optical radiation heats dust grains to high temperatures, followed by their re-emission in infrared (IR) with a peak at $\sim 3 - 30 \mu\text{m}$

(Rees et al. 1969). The broad and excess emission in the mid-IR range, which is called 'infrared bump', is usually observed in the sub-arcsecond scale of numerous AGN and successfully explained by the thermal dust emission from the circumnuclear region (Barvainis 1987, Fritz et al. 2006, Nenkova et al. 2008b, Siebenmorgen et al. 2015). Recently, the high-resolution interferometric observations in mid-IR reveal the significant fraction ($\geq 50 - 80\%$) of mid-IR emission in the extended region along the polar direction of many AGN (Hönig et al. 2012, Hönig et al. 2013, Tristram et al. 2014, López-Gonzaga et al. 2016). Moreover, mid-IR observations with single-dish telescopes at a resolution of $\sim 0.3''$ have detected the thermal emission from warm grains on the scales of 100 pc out to $\sim \text{kpc}$ along the polar direction (Asmus et al. 2014, Asmus et al. 2016). The plausible explanation for the large-scale polar dust is due to radiation pressure on dust (see e.g., Hönig & Kishimoto 2010). Unfortunately, the physical properties of dust grains (size distribution, shape, and composition) in the torus and polar region are not well constrained.

Photometric observations of individual AGN usually report the 'red tail' in its spectrum energy distribution (Webster et al. 1995, Brotherton et al. 2001, Richards et al. 2002), which can be explained by the extinction of dust in the host galaxies (Richards et al. 2003). The observed extinction curves of these AGN exhibit a steep rise in the far-ultraviolet (FUV) range and can be described by the Small Magellanic Clouds (SMC)-like dust model. For example, Richards et al. (2003) found that 273 over 4576 quasars in the Sloan Digital Sky Survey (SDSS), appear to be redder and can be explained by the SMC-like extinction curve. Similarly, Hopkins et al. (2004) reported the similar feature for 9655 quasars observed by SDSS and 1887 quasars observed by Two Micron All Sky Survey (2MASS). In addition, several studies of the dust reddening of AGN report the low values of color excess and visual extinction per gas column density, $E(B - V)/N_{\text{H}}$ and $A_{\text{V}}/N_{\text{H}}$, compared to the standard values produced by interstellar grains (Reichert et al. 1985, Granato et al. 1997, Maiolino et al. 2001). The origin of such low values is unclear.

The steep far-UV rise in the extinction curves requires an enhancement of small grains of size $a \leq 0.1 \mu\text{m}$ in the local environment of AGN compared to the standard interstellar dust model (Mathis et al. 1977, Weingartner & Draine 2001). This feature suggests the modification of dust by the intense radiation field of AGN. Thermal sublimation of AGN dust was first studied by Laor & Draine (1993) for the polar cone and Barvainis (1987) for the torus region. They found that polar and torus grains can be heated to the sublimation temperatures and evaporate near the center of AGN. However, this mechanism is more efficient in destroying small grains than large grains, and it converts small grains directly to the gas phase, which reduces the overall extinction. Dust destruction by Coulomb explosion induced by energetic photons (e.g., X-ray and extreme UV, Draine & Salpeter 1979) was studied by Weingartner et al. (2006) and recently by Tazaki et al. (2020) for AGN. This process also works effectively for very small grains because they can only accommodate a small amount of charge. Lately, Tazaki & Ichikawa (2020) proposed a new scenario of drift-induced sputtering that can remove sub-micron grains in the polar direction. However, this mechanism is not effective enough to enhance small grains as required to reproduce a steep far-UV rise extinction curve. Thus, the origin of such a dominance of small grains in AGN is still unclear.

Recently, Hoang et al. (2019) introduced a new dust destruction mechanism of dust in intense radiation fields, namely RAdiative Torque Disruption (RATD). The mechanism is based on the fact that centrifugal

stress within a dust grain that is spun up to extremely fast rotation by radiative torques (Draine & Weingartner 1996; Lazarian & Hoang 2007; Hoang & Lazarian 2009) can exceed the maximum tensile strength of the material. As a result, rapidly spinning grains can be disrupted into small fragments (see Hoang 2020 for a review). As shown in Hoang et al. (2019), large grains of $a \geq 0.1 \mu\text{m}$ exposed to a strong radiation field can be quickly disrupted into smaller ones even at large distances from the source. We expect that RATD can explain the dominance of small grains around AGN. Thus, the goal of this paper is to quantify the effect of RATD and model the observed extinction curves in the presence of RATD.

The structure of the paper is as follows. In Section 2, we present the radiation field of AGN and briefly describe the RATD mechanism that determines the grain size distribution. The physical model of the polar cone and the dusty torus, and the radiative transfer modeling, are presented in Sections 3 and 4, respectively. We present our numerical results for the dust disruption and the corresponding extinction curves in Sections 5 and 6. An extended discussion and a summary of our main findings are presented in Sections 7 and 8, respectively.

2. THE RATD MECHANISM FOR AGN

2.1. Spectral energy distribution of AGN

The spectral luminosity, L_{λ} , of an unobscured AGN can be described by a power law function with different slopes for different ranges of wavelength as follows (Stalevski et al. 2012):

$$\lambda L_{\lambda} = \alpha \left\{ \begin{array}{ll} 0.158 (\lambda/1 \mu\text{m})^{1.2} & \text{if } 0.001 \mu\text{m} \leq \lambda \leq 0.01 \mu\text{m} \\ 6.3 \times 10^{-4} (\lambda/1 \mu\text{m}) & \text{if } 0.01 \mu\text{m} < \lambda \leq 0.1 \mu\text{m} \\ 2 \times 10^{-4} (\lambda/1 \mu\text{m})^{-0.5} & \text{if } 0.1 \mu\text{m} < \lambda \leq 5 \mu\text{m} \\ 0.011 (\lambda/1 \mu\text{m})^{-3} & \text{if } 5 \mu\text{m} < \lambda \leq 50 \mu\text{m} \end{array} \right\} (1)$$

where α is a normalization constant, which is determined by the bolometric luminosity. We consider an AGN with a constant bolometric luminosity of $L_{\text{bol}} = 10^{46} \text{erg s}^{-1}$ and disregard their time variability.

To model the grain disruption by RATD in AGN environments, we only consider photons with wavelengths from $\lambda_1 = 0.1 \mu\text{m}$ to $\lambda_2 = 20 \mu\text{m}$, where the lower limit is determined by the Lyman limit (i.e., photons of $\lambda < 0.1 \mu\text{m}$ are entirely absorbed by hydrogen), and the upper limit is chosen such that above this wavelength the RAT efficiency is negligible for interstellar grains of size $a \lesssim 1 \mu\text{m}$. The strength of the radiation field is defined as $U = u_{\text{rad}}/u_{\text{ISRF}}$, where u_{rad} is the energy density of the assumed radiation spectrum (Equation 1), and $u_{\text{ISRF}} = 8.64 \times 10^{-13} \text{erg cm}^{-3}$ is the energy density

of the average interstellar radiation field (ISRF) in the solar neighborhood (Mathis et al. 1983).

The mean wavelength of the radiation field considered for RATD is given by:

$$\bar{\lambda} = \frac{\int_{\lambda_1}^{\lambda_2} \lambda L_{\lambda} d\lambda}{\int_{\lambda_1}^{\lambda_2} L_{\lambda} d\lambda}, \quad (2)$$

and we get $\bar{\lambda} = 0.876 \mu\text{m}$ with the usage of L_{λ} from Equation (1).

2.2. The RATD mechanism

An irregular dust grain exposed to an anisotropic radiation field experiences radiative torques due to differential scattering and absorption of left-handed and right-handed photons (Draine & Weingartner 1996, Lazarian & Hoang 2007). In an intense radiation field, the grain can be spun up to extremely fast rotation so that it is disrupted into small fragments when the centrifugal stress exceeds the maximum tensile strength of the grain material (Hoang et al. 2019). This mechanism is named RAdiative Torque Disruption mechanism (RATD, see Hoang et al. 2019 for details). Here, we briefly summarize the main formulae for reference.

Let a be the effective size of an irregular grain, which is defined as the radius of an equivalent spherical grain with the same volume as the irregular grain. The angular velocity of the irregular grain spun-up by RATs is obtained by solving the equation of motion (Hoang et al. 2019):

$$\frac{I d\omega}{dt} = \Gamma_{\text{RAT}} - \frac{I\omega}{\tau_{\text{damp}}}, \quad (3)$$

where $I = 8\pi\rho a^5/15$ is the grain inertia moment with ρ the grain mass density, τ_{damp} is the characteristic timescale of grain rotational damping (see Hoang et al. 2019 for details). The first term of the right-hand side Γ_{RAT} is the radiative torque arising from the interaction of the anisotropic radiation field of AGN with grain of size a , which equals:

$$\begin{aligned} \Gamma_{\text{RAT}} &= \int_{\lambda_1}^{\lambda_2} \Gamma_{\lambda} d\lambda \\ &= \int_{\lambda_1}^{\lambda_2} \pi a^2 \gamma_{\text{rad}} u_{\lambda,0} e^{-\tau_{\lambda}} \left(\frac{\lambda}{2\pi} \right) Q_{\lambda} d\lambda. \end{aligned} \quad (4)$$

In above equation, $u_{\lambda,0} = L_{\lambda,0}/(4\pi cd^2)$ is the intrinsic energy density at wavelength λ with intrinsic spectral luminosity given by Equation (1), τ_{λ} is the optical depth, and γ_{rad} is the anisotropy degree of the radiation field ($0 \leq \gamma_{\text{rad}} \leq 1$). Here, we adopt $\gamma_{\text{rad}} = 1$ for the unidirectional radiation field of AGN. Q_{λ} is the RAT

efficiency at wavelength λ , which is (Hoang & Lazarian 2008, Hoang & Lazarian 2014, Hoang et al. 2019):

$$Q_{\lambda} = \begin{cases} \approx 2.33 \left(\frac{\lambda}{a}\right)^{-3} & \text{for } a \lesssim \lambda/1.8 \\ \approx 0.4 & \text{for } a > \lambda/1.8 \end{cases}. \quad (5)$$

In the constant radiation field, the grain of size a will be spun-up continuously by a constant radiative torque, Γ_{RAT} , and achieve a maximum angular speed of ω_{RAT} after about a damping timescale. An analytical formula for ω_{RAT} as follows:

$$\omega_{\text{RAT}} = \frac{\Gamma_{\text{RAT}} \tau_{\text{damp}}}{I}. \quad (6)$$

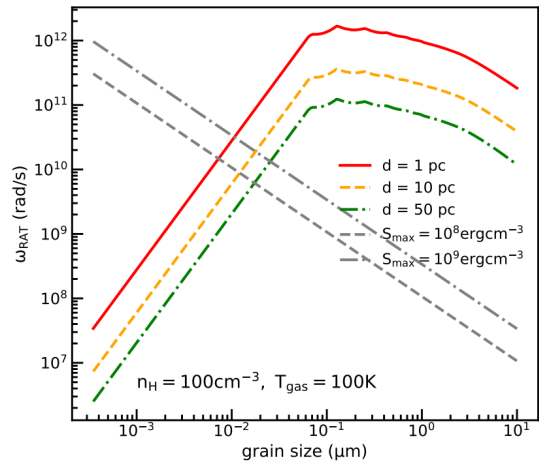


Figure 1. Maximum angular speed of grains spun-up by RATs due to AGN radiation as a function of the grain size for different distances d to the central source. The gray dashed lines show the disruption speed for grains with $S_{\text{max}} = 10^8$ and 10^9 erg cm^{-3} . Optically thin environment with the gas density of $n_{\text{H}} = 100 \text{ cm}^{-3}$ and the gas temperature of $T_{\text{gas}} = 100 \text{ K}$ are assumed. The intersection of ω_{RAT} and ω_{disr} determines the disruption size.

Figure 1 shows the variation of the maximum angular speed due to RATs, ω_{RAT} , with the grain size from $a = 0.001 \mu\text{m}$ to $10 \mu\text{m}$ at different distances to the center of AGN in the absence of dust reddening, with a gas density of $n_{\text{H}} = 100 \text{ cm}^{-3}$ and gas temperature of $T_{\text{gas}} = 100 \text{ K}$. At the same distance, ω_{RAT} increases with the grain size to the peak at $a \sim 0.2 - 0.5 \mu\text{m}$ then decreases for larger grains. The reason is as follows: for grains of $a \leq 0.2 \mu\text{m}$, smaller grains receive less energy due to smaller cross section πa^2 and smaller RAT efficiency Q_{λ} from the considered spectrum (see Equation 5). Thus, they are spun up to lower ω_{RAT} compared with larger grains. On the contrary, grains of $a \geq 0.2 \mu\text{m}$ nearly experience the same RAT efficiency that larger grains

will be spun-up to lower ω_{RAT} due to larger mass. For example, at $d = 10$ pc, grains of $a = 0.001 \mu\text{m}$, $0.01 \mu\text{m}$ and $a = 0.1 \mu\text{m}$ are spun up to $\omega_{\text{RAT}} \sim 3 \times 10^7 \text{ rad s}^{-1}$, $\sim 10^{10} \text{ rad s}^{-1}$ and $3 \times 10^{11} \text{ rad s}^{-1}$, respectively. This value decreases to $\omega_{\text{RAT}} \sim 10^{10} \text{ rad s}^{-1}$ for micron-sized grains of $a \geq 1 \mu\text{m}$. In addition, grains which are far from the center of AGN receive lower radiation flux and rotate slower.

The rapidly spinning grain will be disrupted into small fragments when its centrifugal stress $S = \rho a^2 \omega^2 / 4$ exceeds the maximum tensile strength of the grain material, S_{max} . The value of S_{max} depends on the grain material, internal structure, and perhaps the grain size, i.e., large grains usually have porous structure with lower value of S_{max} compared with small grains with compact structure. It can vary from $S_{\text{max}} = 10^{11} \text{ erg cm}^{-3}$ for ideal materials, i.e., diamond (Burke & Silk 1974; Draine & Salpeter 1979) to $S_{\text{max}} \sim 10^9 - 10^{10} \text{ erg cm}^{-3}$ for polycrystalline bulk solid (Hoang et al. 2019) and $S_{\text{max}} \sim 10^6 - 10^8 \text{ erg cm}^{-3}$ for composite grains (Hoang 2019). In this paper, we take $S_{\text{max}} = 10^8 \text{ erg cm}^{-3}$ as a typical value.

The critical angular speed at which rotational disruption occurs is obtained by setting S equal to S_{max} , which yields:

$$\omega_{\text{disr}} = \frac{2}{a} \left(\frac{S_{\text{max}}}{\rho} \right)^{1/2}. \quad (7)$$

Then, the grain disruption size, i.e., a_{disr} , at which all larger grains are fragmented to smaller pieces by RATD, can be calculated by setting $\omega_{\text{disr}} = \omega_{\text{RAT}}$. In Figure 1, the gray dashed and dashed-dot line present the dependence of the critical angular speed ω_{disr} with the grain size. One can see that for the same internal strength, small grains are required to be spun up to higher angular speed in order to be disrupted by RATD. Thus, at the same distance, large grains are easier to be disrupted by RATD due to its higher ω_{RAT} and lower ω_{disr} , i.e., the right-hand side of the intersection where $\omega_{\text{RAT}} = \omega_{\text{disr}}$. For example, at $d = 10$ pc for grains with $S_{\text{max}} = 10^8 \text{ erg cm}^{-3}$, all large grains of $a \geq 0.02 \mu\text{m}$ are destroyed by RATD, while smaller grains can survive. Grains at large distances to AGN are less affected by RATD due to lower radiation energy density, i.e., lower ω_{RAT} . Similarly, grains with higher S_{max} are more difficult to be broken due to its higher disruption threshold ω_{disr} (see Equation 7 and dashed-dot gray line).

Note that the decrease of ω_{RAT} with grain sizes for large grains of $a \geq 0.1 \mu\text{m}$ will set an upper limit at which all larger grains are not affected by RATD, which is denoted by $a_{\text{disr,max}}$. From Figure 1, one can see that micron-sized grains are disrupted totally by RATD in

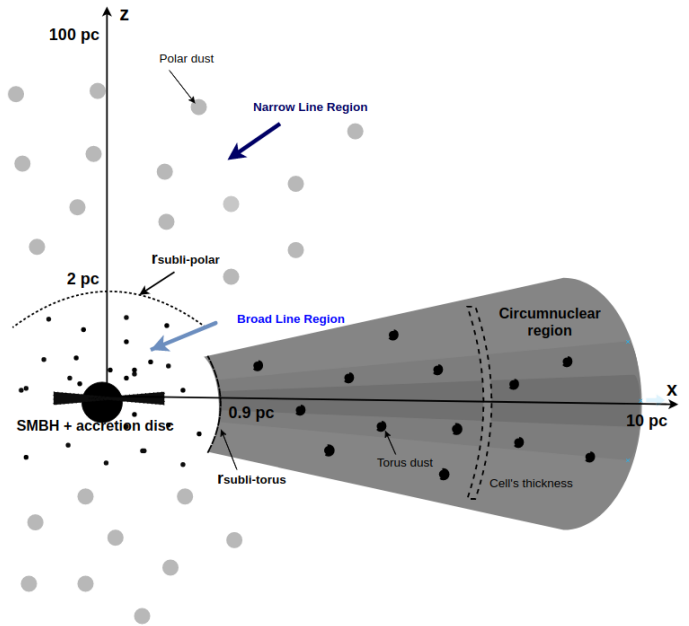


Figure 2. A two-dimensional illustration of an axisymmetric structure of AGN. The central engine including the SMBH and an accretion disk (black circle and small black flared disk) is covered by a dusty toroidal region on the equatorial plane and an ionized region (BLR, NLR) extending along the polar direction. We consider that the torus region has the ‘flared disc’ geometry (Fritz et al. 2006).

The inner boundary of the polar cone and torus are determined by the sublimation distances $r_{\text{subli-polar}}$ and $r_{\text{subli-torus}}$, beyond which grains are not sublimated by AGN radiation. To model the dust destruction by RATs, we divide the polar cone and torus into spherical cells of the same thickness, d_{cell} (dashed donut shape). The distance of each cell toward the center of AGN is denoted by r , and Θ is the observed angle.

the optically thin environments. However, in the dense regions, the strong attenuation of the radiation field may reduce the value of $a_{\text{disr,max}}$ that let more micron-sized grains survive (see Hoang et al. 2020 for a detailed explanation).

3. A PHYSICAL MODEL OF AGN

Figure 2 shows a schematic illustration of the AGN structure. The central engine, including a supermassive black hole (SMBH) and an accretion disk in the center of AGN, is presented by a black circle and a black flared disk in the center of the figure. This region is covered by the dusty toroidal structure on the equatorial plane (gray region) and the scattering region, i.e., BLR and NLR, along the polar direction. The exact geometry of torus region has not yet been constrained. Therefore, in this paper, we consider a simple but realistic geometry of a ‘flared disc’ to be the shape of torus region (Fritz

et al. 2006, Efstathiou & Rowan-Robinson 1995). The innermost locations of dust in the polar cone and torus toward the AGN center are determined by the sublimation distances $r_{\text{subli-polar}}$ and $r_{\text{subli-torus}}$, respectively, which constitute sublimation fronts. Thus, grains can survive in the intense radiation field of AGN beyond the sublimation fronts.

3.1. Polar cone

The presence of dust along the polar direction can arise from a magneto-hydrodynamical wind from the central engine of AGN or radiation pressure. Close to the center, grains are quickly heated to the high temperature and sublimated to the gas phase (Laor & Draine 1993). The radius at which the grain temperature equals the sublimation threshold is called the sublimation distance, $d_{\text{subli-polar}}$. The exact value of $d_{\text{subli-polar}}$ depends on the size and composition of grains. In general, small grains are destroyed to larger distances due to their low heat capacity. Silicate grains are destroyed more efficiently than carbonaceous grains due to their lower sublimation temperature (see Laor & Draine 1993 for details). For example, from Figure 8 in Laor & Draine (1993), polar silicate grains of size $a \geq 0.005 \mu\text{m}$ can start to survive around AGN with $L_{\text{bol}} = 10^{45} \text{ erg s}^{-1}$ beyond the outer boundary of BLR of $d \sim 4 \text{ pc}$, while it is $d \sim 1 \text{ pc}$ for carbonaceous grains of size $a \geq 0.005 \mu\text{m}$. Thus, we adopt the average value of $r_{\text{subli-polar}} = 2 \text{ pc}$ to be the sublimation distance of both silicate and carbonaceous grains in the polar direction.

The gas number density of the polar region can be described by a power law (Laor & Draine 1993):

$$n_{\text{H,polar}}(r) = n_{\text{H}}^0 \left(\frac{r}{r_{\text{subli-polar}}} \right)^{\gamma_{\text{polar}}}, \quad (8)$$

where n_{H}^0 is the gas density at $r = r_{\text{subli-polar}}$, and γ_{polar} is the power-law index of the distribution. The value of γ_{polar} varies from $\gamma_{\text{polar}} = 0$ (corresponding to a uniform distribution) to $\gamma_{\text{polar}} = -2$ (Lyu & Rieke 2018).

Gas in the polar region is strongly ionized due to the intense UV radiation of AGN. The ionization parameter is defined by:

$$\begin{aligned} U_{\text{ion}} &= \frac{n_{\gamma}(\geq 13.6 \text{ eV})}{n_{\text{H}}} \\ &= \frac{1}{n_{\text{H}}} \int_{13.6 \text{ eV}}^{1 \text{ keV}} \frac{u_{\lambda}}{E_{\lambda}} d\lambda, \end{aligned} \quad (9)$$

where $n_{\gamma}(\geq 13.6 \text{ eV})$ is the number density of ionizing photons of energy of $13.6 \text{ eV} \leq E_{\lambda} \leq 1 \text{ keV}$ with $E_{\lambda} = hc/\lambda$, and u_{λ} is the spectral energy density given

by Equation (1). We can neglect the reduction of ionizing photons by neutral hydrogen due to its negligible fraction (i.e., $n(\text{H}^+) \sim n_{\text{H}}$).

The gas temperature T_{gas} in the polar cone is thus determined by the balance between photoionization heating and radiative cooling, which follows (Yu, Sazonov et al. 2004, Sazonov et al. 2005, Weingartner et al. 2006):

$$T_{\text{gas}} = \begin{cases} 10^4 \text{ K} & \text{if } U_{\text{ion}} \leq 2 \\ 5 \times 10^3 U_{\text{ion}} \text{ K} & \text{if } 2 < U_{\text{ion}} \leq 4 \times 10^3 \\ 2 \times 10^7 \text{ K} & \text{if } U_{\text{ion}} > 4 \times 10^3 \end{cases} \quad (10)$$

3.2. Dusty torus

Similar to the polar cone, grains in the torus region start to survive beyond the sublimation distance where the dust temperature drops below $T_{\text{subli}} \sim 1500 \text{ K}$. From the study of Hönig & Kishimoto (2010), we adopt the sublimation distance of $r_{\text{subli-torus}} = 0.9\sqrt{(L_{\text{bol},46})}$ (pc) with $L_{\text{bol},46} = L_{\text{bol}}/(10^{46} \text{ erg s}^{-1})$. The torus structure and the morphology of grains in the circumnuclear region are still not constrained. Initially, Krolik & Begelman (1988) suggested that grains might concentrate into a clumpy structure to avoid being destroyed by the intense radiation field of AGN. However, the difficulty in performing the clumpy model appeals to the simple case of the smooth distribution with different vertical and horizontal profiles (Efstathiou & Rowan-Robinson 1995, Manske et al. 1998, Fritz et al. 2006). Nevertheless, the smooth distribution cannot explain the depletion of silicate absorption feature at $9.7 \mu\text{m}$ in type 1 AGN and the broad observed far-IR emission compared to the modeling (Granato et al. 1997, Granato & Danese 1994). Rowan-Robinson (1995) suggested solving these problems by assuming the concentration of grains in the clumpy structure and this idea was confirmed by Nenkova et al. (2002). The clumpy model is also supported by observations of the inhomogeneous circumnuclear region (Tristram et al. 2007). The detailed model of the clumpy structure is then developed to solve the radiative transfer and compare with observations (e.g., Nenkova et al. 2002, Nenkova et al. 2008a, Nenkova et al. 2008b, Dullemond & van Bemmelen 2005 (two-dimension), Hönig et al. 2006, Stalevski et al. (2012), Siebenmorgen et al. (2015) (three-dimension)).

In this paper, our main goal is to explore the effect of rotation disruption on polar and torus dust grains and to understand how it changes the dust extinction of AGN. Therefore, we adopt the simple smooth dust distribution model in the flared disk taken from Fritz et al. (2006), and modeling with a more realistic clumpy AGN structure will be addressed in our future study.

We consider a spherical coordinate system $(r, \Theta, \phi = 0^\circ)$ in the x-z plane. The gas number density in the torus (see Figure 2) can be described by (Fritz et al. 2006):

$$n_{\text{H,torus}}(r, \Theta) = n_{\text{H}}^0 \left(\frac{r}{r_{\text{subli-torus}}} \right)^{\gamma_{\text{torus}}} e^{\beta \cos(\Theta)}, \quad (11)$$

where γ_{torus} and β are the power-law index of the gas density profile along the radial direction r and polar direction, (i.e., the observed angle Θ), respectively, and n_{H}^0 is the gas density at the sublimation front of $r = r_{\text{subli-torus}}$.

In the dense torus, dust and gas are essentially in thermal equilibrium (see other studies for dense regions like protoplanetary disks (Tung & Hoang 2020) and dense molecular clouds (Hoang et al. 2021)). The gas temperature can be obtained by the equilibrium temperature of grains, which is given by (Draine 2011):

$$T_{\text{dust}} \approx 16.4U^{1/6} \text{ K}, \quad (12)$$

where U is the radiation field strength.

4. RADIATIVE TRANSFER MODELLING

4.1. Grain model

Radiation emitting from AGN is attenuated due to scattering and absorption by surrounding dust. To calculate the dust extinction, we adopt a popular ISM mixed-dust model consisting of astronomical silicate and carbonaceous grains (see Li & Draine 2001, Weingartner & Draine 2001, Draine & Li 2007). We assume that grains in AGN follow a power-law size distribution with a slope α :

$$\frac{dn^j}{da} = C^j n_{\text{H}} a^\alpha, \quad (13)$$

where C^j is the normalization constant which is determined by the dust-to-gas mass ratio η :

$$\eta = \frac{4\pi}{3m_{\text{H}}} \frac{(a_{\text{max}}^{4+\alpha} - a_{\text{min}}^{4+\alpha})}{4 + \alpha} \sum_{j=\text{sil,carb}} C^j \rho^j, \quad (14)$$

where ρ^j is the mass density of component j , we take $\rho_{\text{sil}} = 3.5 \text{ g cm}^{-3}$, $\rho_{\text{carb}} = 2.2 \text{ g cm}^{-3}$ and $C_{\text{sil}}/C_{\text{carb}} = 1.12$ (Draine & Lee 1984, Laor & Draine 1993). Without RATD, we consider the range of grain sizes from $a_{\text{min}} = 3.5 \text{ \AA}$ to $a_{\text{max}} = 10 \text{ \mu m}$ with $\alpha = -3.5$ (Mathis et al. 1977). When increasing the maximum grain size to 10 \mu m , the total dust mass will be higher than the standard dust model in our Galaxy. Thus, the original value of normalization constant C_{sil} and C_{carb} from Mathis et al. (1977) must be reduced by a factor of 7

to keep the Galactic standard dust-to-gas mass ratio of $\eta = 0.01$. The new values are $C_{\text{sil}} = 1.16 \times 10^{-26} \text{ cm}^{2.5}$ and $C_{\text{carb}} = 1.036 \times 10^{-26} \text{ cm}^{2.5}$, for silicate and carbonaceous grains, respectively.

When we account for the effect of RATD, the grain sizes from a_{disr} to $a_{\text{disr,max}}$ will be fragmented to smaller sizes, resulting in the two separated grain size distributions. The first one is the range of grain sizes of $a_{\text{disr,max}} - a_{\text{max}}$ that still follows the MRN distribution with $\alpha = -3.5$. The second one is the grain sizes from a_{min} to a_{disr} that follows a steeper distribution with a new slope α due to the enhancement of small grains by RATD. By assuming the normalization constant of silicate and carbonaceous grains C_{sil} and C_{carb} to be a constant, the new grain size distribution of small grains can be found from the conservation of dust mass, which follows (see Giang et al. 2020 for details):

$$\frac{a_{\text{disr,max}}^{4-3.5} - a_{\text{min}}^{4-3.5}}{4 - 3.5} = \frac{a_{\text{disr}}^{4+\alpha} - a_{\text{min}}^{4+\alpha}}{4 + \alpha}. \quad (15)$$

4.2. Effect of dust reddening in the presence of RATD

The emergent spectral energy density (u_λ) of AGN radiation after traveling through a dusty cloud of thickness d is given by

$$u_\lambda = u_{\lambda,0} e^{-\tau_\lambda}, \quad (16)$$

where $u_{\lambda,0} = L_{\lambda,0}/(4\pi cd^2)$ is the intrinsic spectral energy density given by Equation (1), and τ_λ is the optical depth induced by intervening grains.

In the absence of RATD, AGN radiation is attenuated by all grains from a_{min} to a_{max} following the MRN distribution. When RATD is included, AGN radiation will be attenuated by two dust populations following different size distributions as described in Section 4.1. The extinction cross section per H by dust at distance r at wavelength λ in units of cm^2/H is then calculated as (Hoang et al. 2013):

$$\begin{aligned} \sigma_{\text{ext}}(\lambda, r) &= \sum_{j=\text{sil,carb}} \int Q_{\text{ext}}^j(a) \pi a^2 \frac{dn^j}{da}(r) da \\ &= \sum_{j=\text{sil,carb}} \left(\int_{a_{\text{min}}}^{a_{\text{disr}}(r)} Q_{\text{ext}}^j(a) \pi a^2 a^{\alpha(r)} da \right. \\ &\quad \left. + \int_{a_{\text{disr,max}}(r)}^{a_{\text{max}}} Q_{\text{ext}}^j(a) \pi a^2 a^{-3.5} da \right) C^j, \quad (17) \end{aligned}$$

where Q_{ext} is the extinction efficiency, C^j is the normalization constant for silicate and carbonaceous grains, $a_{\text{disr}}(r)$, $a_{\text{disr,max}}(r)$, and $\alpha(r)$ are the grain disruption size, the maximum grain disruption size, and the new slope of the distribution of small grain size at distance

r . We assume that grains of sizes between a_{disr} and $a_{\text{disr,max}}$ are totally disrupted into grains smaller than a_{disr} . For sub-micron grains, we adopt Q_{ext} calculated for the oblate spheroidal shape with an axial ratio of 2 in Hoang et al. (2013). For micron grains, we calculated Q_{ext} for the same shape using DDSCAT (Draine et al. 1994). The optical depth induced by dust in the cloud of thickness d is:

$$\tau_{\lambda}(d) = \int_0^d \sigma_{\text{ext}}(\lambda, r) n_{\text{H}}(r) dr, \quad (18)$$

where $n_{\text{H}}(r)$ is the gas density at distance r , which is described by Equation (8) for the polar cone and Equation (11) for the torus region.

To numerically model the dust reddening effect, we divide the smooth dusty polar cone and torus (see Section 3) into a number of thin cells of the same thickness of $d_{\text{cell}} = 0.05$ pc (see the dashed donut shape in Figure 2). The thickness of the cell is chosen such that the change of the grain size distribution within the cell is negligible. With this choice, in the i^{th} cell, we can calculate the optical depth produced by grains in the cell $\Delta\tau_{\lambda,i}$ (using Equation 17 and Equation 18 with d replaced by d_{cell}). Thus, the total optical depth produced by dust in the cloud of thickness d containing n dusty cells is then obtained as:

$$\tau_{\lambda,n} = \sum_{i=1}^n \Delta\tau_{\lambda,i}, \quad (19)$$

where $i = 1$ denotes the first cell at the sublimation front, and $i = n$ denotes the last cell at distance d .

5. MODELLING DUST DISRUPTION IN AGN ENVIRONMENT

To model the RATD effect, we first calculate the radiation field strength U as described in Section 4 and solve the equation of motion (Equation 3) to get the terminal angular speed ω_{RAT} for the range of grain size from a_{min} to a_{max} . Then, by comparing ω_{RAT} with the critical angular speed ω_{disr} given by Equation (7), one can determine the range of $a_{\text{disr}} - a_{\text{disr,max}}$ at which grains are disrupted into smaller sizes by RATD.

5.1. Polar cone

The upper panel of Figure 3 shows the variation of the radiation field strength U in the polar cone as a function of distance for different values of initial gas density n_{H}^0 at the sublimation front of $r_{\text{subli-polar}} = 2$ pc, assuming the density profile given by Equation (8) with $\gamma_{\text{polar}} = -1$ and the maximum tensile strength

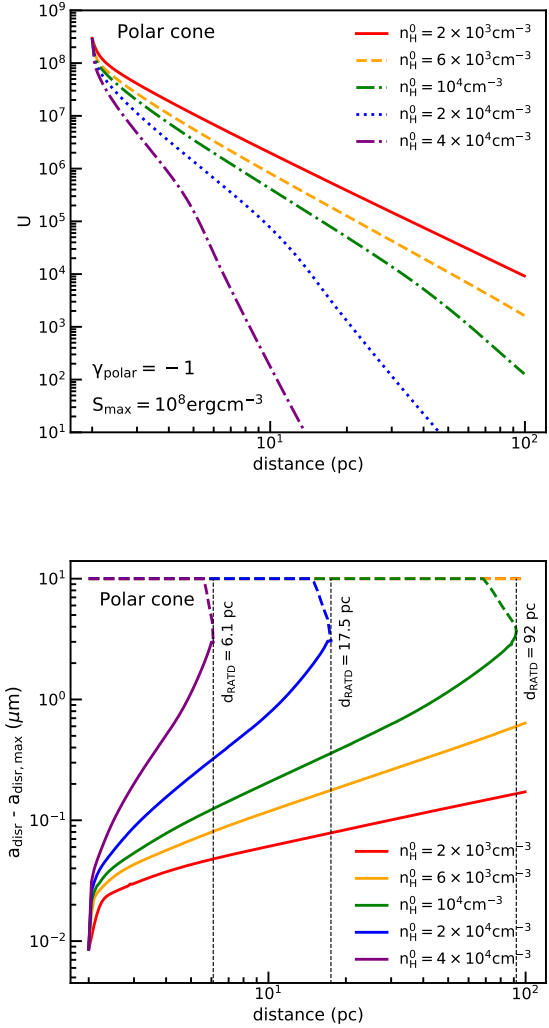


Figure 3. Variation of the radiation field strength, U (upper panel), and the range of grain sizes of $a_{\text{disr}} - a_{\text{disr,max}}$ which are disrupted by RATD (solid and dashed lines) (lower panel) with the cloud distances in the polar cone, assuming different initial gas density n_{H}^0 , $\gamma_{\text{polar}} = -1$, and $S_{\text{max}} = 10^8 \text{ erg cm}^{-3}$.

of $S_{\text{max}} = 10^8 \text{ erg cm}^{-3}$. The lower panel shows the corresponding range of grains which are disrupted by RATD, starting from the grain disruption size a_{disr} (solid lines) to the end at the maximum grain disruption size $a_{\text{disr,max}}$ (dashed lines).

For all considered gas density profiles, one can see that grains are not affected by RATD if they are very far from the center of AGN. It arises from the strong attenuation of AGN radiation such that it is not strong enough to spin up any grains to the disruption threshold. In this case, the grain disruption size is set to the maximum grain size. The distance where RATD ceases determines the boundary of the active region of RATD, denoted by

d_{RATD} and marked by the vertical black dashed line. As the distance to AGN decreases, grains are spun up to faster rotation due to higher radiation flux, resulting in the expansion of the size range of disrupted grains. For example, with $n_{\text{H}}^0 = 10^4 \text{ cm}^{-3}$, the disruption range expands continuously from $a_{\text{disr}} = a_{\text{disr,max}}$ at $d = 100$ pc (no disruption) to $1 - 10 \mu\text{m}$ at ~ 40 pc and $0.1 - 10 \mu\text{m}$ at ~ 5 pc.

For a higher value of n_{H}^0 , the radiation strength is decreased more drastically due to stronger dust reddening, decreasing the RATD efficiency (i.e., smaller active region of RATD). For instance, the value of d_{RATD} reduces continuously from $d_{\text{RATD}} = 92$ pc to 17.5 pc and 6.1 pc if the initial gas density increases from $n_{\text{H}}^0 \leq 10^4 \text{ cm}^{-3}$ to $2 \times 10^4 \text{ cm}^{-3}$ and $4 \times 10^4 \text{ cm}^{-3}$, respectively.

The upper panel of Figure 4 shows the range of disrupted grains within 100 pc in the polar cone for different values of the power-law index γ_{polar} , assuming $n_{\text{H}}^0 = 10^4 \text{ cm}^{-3}$ and $S_{\text{max}} = 10^8 \text{ erg cm}^{-3}$. For the same initial gas density, the slower decrease of n_{H} with distances, i.e., larger γ_{polar} , induces stronger attenuation of AGN radiation and reduces the active region of RATD. For example, d_{RATD} reduces from $d = 92$ pc to 37.5 pc and 18.5 pc if γ_{polar} increases from ≤ -1 to -0.8 and -0.5, respectively.

The lower panel of Figure 4 shows the same as the upper panel but for different tensile strengths, assuming $n_{\text{H}}^0 = 10^4 \text{ cm}^{-3}$ and $\gamma_{\text{polar}} = -1$. One can see that with the same gas density profile, grains with higher S_{max} are less disrupted by RATD due to its higher disruption threshold ω_{disr} (see Equation 7). For example, compact grains of $S_{\text{max}} = 10^{10} \text{ erg cm}^{-3}$ and $S_{\text{max}} = 10^9 \text{ erg cm}^{-3}$ are only destroyed within 13.5 pc and 33 pc, while composite grains with $S_{\text{max}} \leq 10^8 \text{ erg cm}^{-3}$ can be disrupted up to $d_{\text{RATD}} \geq 92$ pc.

5.2. Torus region

Figure 5 shows the variation of the radiation field strength U on the equatorial plane of the torus with distances (upper panel) and the corresponding size range of grains disrupted by RATD (lower panel). The number gas density in the torus is computed by Equation (11) with $\gamma_{\text{torus}} = -1$, $\beta = -2$, $\Theta = 90^\circ$. The maximum tensile strength of grains is $S_{\text{max}} = 10^8 \text{ erg cm}^{-3}$. Similar to the polar cone, the radiation field strength is decreased stronger in the dense torus region (i.e., higher n_{H}^0), which shrinks the active region of RATD. For example, the disruption region decreases from $\lesssim 9.35$ pc to 3.1 pc and 1.7 pc when the initial gas density increases from $n_{\text{H}}^0 = 10^5 \text{ cm}^{-3}$ to $2 \times 10^5 \text{ cm}^{-3}$ and $4 \times 10^5 \text{ cm}^{-3}$, respectively.

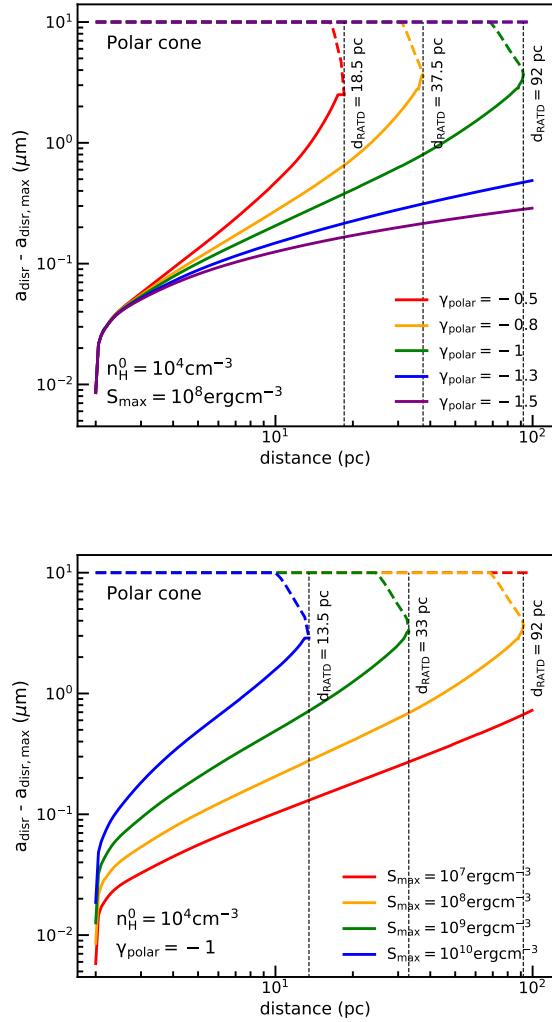


Figure 4. The same as Figure 3 but for different power-law indexes γ_{polar} , assuming $n_{\text{H}}^0 = 10^4 \text{ cm}^{-3}$ and $S_{\text{max}} = 10^8 \text{ erg cm}^{-3}$ (upper panel), and for different maximum tensile strengths S_{max} , assuming $n_{\text{H}}^0 = 10^4 \text{ cm}^{-3}$ and $\gamma_{\text{polar}} = -1$ (lower panel).

Figure 6 shows the dependence of the RATD efficiency with different parameters of the gas density profile and the maximum tensile strength. The upper left panel is for the varying power-index of the gas distribution in the radial direction γ_{torus} . As increasing γ_{torus} , the gas density drops slower resulting in the stronger dust reddening effect on the radiation field and the weaker effect of RATD in the torus region. For example, with $n_{\text{H}}^0 = 10^5 \text{ cm}^{-3}$, the active region of RATD on the equatorial plane (i.e., $\Theta = 90^\circ$) reduces from 9.35 pc to 6.1 pc and 4.2 pc if the slope of the gas density profile becomes shallower from $\gamma_{\text{torus}} = -1$ to -0.8 and -0.5, respectively.

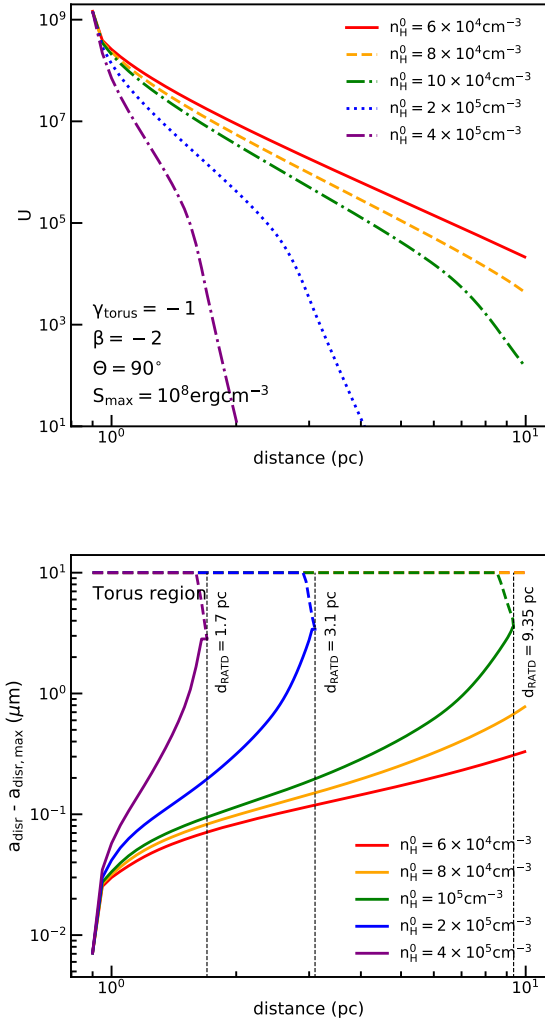


Figure 5. Variation of the radiation field strength U (upper panel) and the range of grain sizes which are disrupted by RATD (lower panel) with distance within 10 pc from the center AGN on the equatorial plane ($\Theta = 90^\circ$) for the torus, assuming different initial gas densities n_{H}^0 , $\gamma_{\text{torus}} = -1$, $\beta = -2$ and $S_{\text{max}} = 10^8 \text{ erg cm}^{-3}$.

The upper right panel shows the results for the different values of S_{max} . As increasing S_{max} , the RATD is decreased due to larger disruption limit, which shrinks the disruption zone. For instance, with $n_{\text{H}}^0 = 10^5 \text{ cm}^{-3}$ and for grains on the equatorial plane, d_{RATD} shrinks from ≥ 10 pc to 3.9 pc with increasing the strength from $S_{\text{max}} \leq 10^8 \text{ erg cm}^{-3}$ to $10^{10} \text{ erg cm}^{-3}$.

The lower left panel shows the results for different observed angles Θ . The active region of RATD expands when the observed direction is varied from the edge-on view ($\Theta = 90^\circ$) to the face-on view (e.g., $\Theta = 30^\circ$), due to the quick drop of gas density above the equatorial

plane. The fast decrease of the gas density in the polar direction due to a lower value of β also increases the active zone of RATD (see the lower right panel). For instance, with $n_{\text{H}}^0 = 2 \times 10^5 \text{ cm}^{-3}$ and $\beta = -2$, RATD only can modify dust within $d \leq 3.1$ pc on the equatorial plane, but it can remove large grains within $d \leq 6.65$ pc along the direction of $\Theta = 75^\circ$ and $d \geq 10$ pc for $\Theta > 60^\circ$. Moreover, along the direction of $\Theta = 75^\circ$, the active region of RATD can increase from 6.65 pc to > 10 pc when the gas density drops with distances with $\beta \leq -3$.

6. MODELLING PHOTOMETRIC PARAMETERS WITH RATD EFFECT

6.1. Extinction curves

Now, we use the new grain size distribution obtained by RATD to model extinction curves toward AGN. To account for the fact that AGN may have a clumpy structure, we will model both the extinction cross section induced by grains in the dusty cell at different distances and the final extinction curve produced by all grains from the sublimation front.

From the numerical calculation of the optical depth described in Section 4.2, the dust extinction at wavelength λ induced by grains from the sublimation distance to n^{th} cell, $A(\lambda, n)$, is given by:

$$A(\lambda, n) = \sum_{i=1}^n 1.086 \Delta \tau_{\lambda, i} \text{ mag}, \quad (20)$$

where $\Delta \tau_{\lambda, i}$ is the optical depth produced by the i^{th} cell.

6.1.1. Polar cone

The left panel of Figure 7 shows the extinction cross section per H, $\sigma_{\text{ext}}(\lambda)$, produced by grains in a cell at different distances from $d = 100$ pc to 2 pc in the polar region, assuming $n_{\text{H}}^0 = 10^4 \text{ cm}^{-3}$ and $S_{\text{max}} = 10^8 \text{ erg cm}^{-3}$. Here, we assume that the cell is thin such that the grain disruption size does not change substantially in the cell. The gray dashed line is the wavelength-dependent extinction cross section produced by original grains that follows the MRN distribution. At a distance of $d = 100$ pc, carbonaceous micron-sized grains still be enhanced by RATD because of smaller dust mass density (see Equation 6). Thus, one can obtain the higher extinction cross section by grains from FUV to MIR compared with ones produced by the original dust model. As the distance decreases to $d = 2$ pc, the efficiency of RATD increases due to the increase of radiation flux. As a result, $\sigma_{\text{ext}}(\lambda)$ at optical-MIR continues to rise due to the enhancement of sub-micron grains, i.e., the curve at 75 pc, 45 pc, 45 pc, 25 pc, then decreases later when

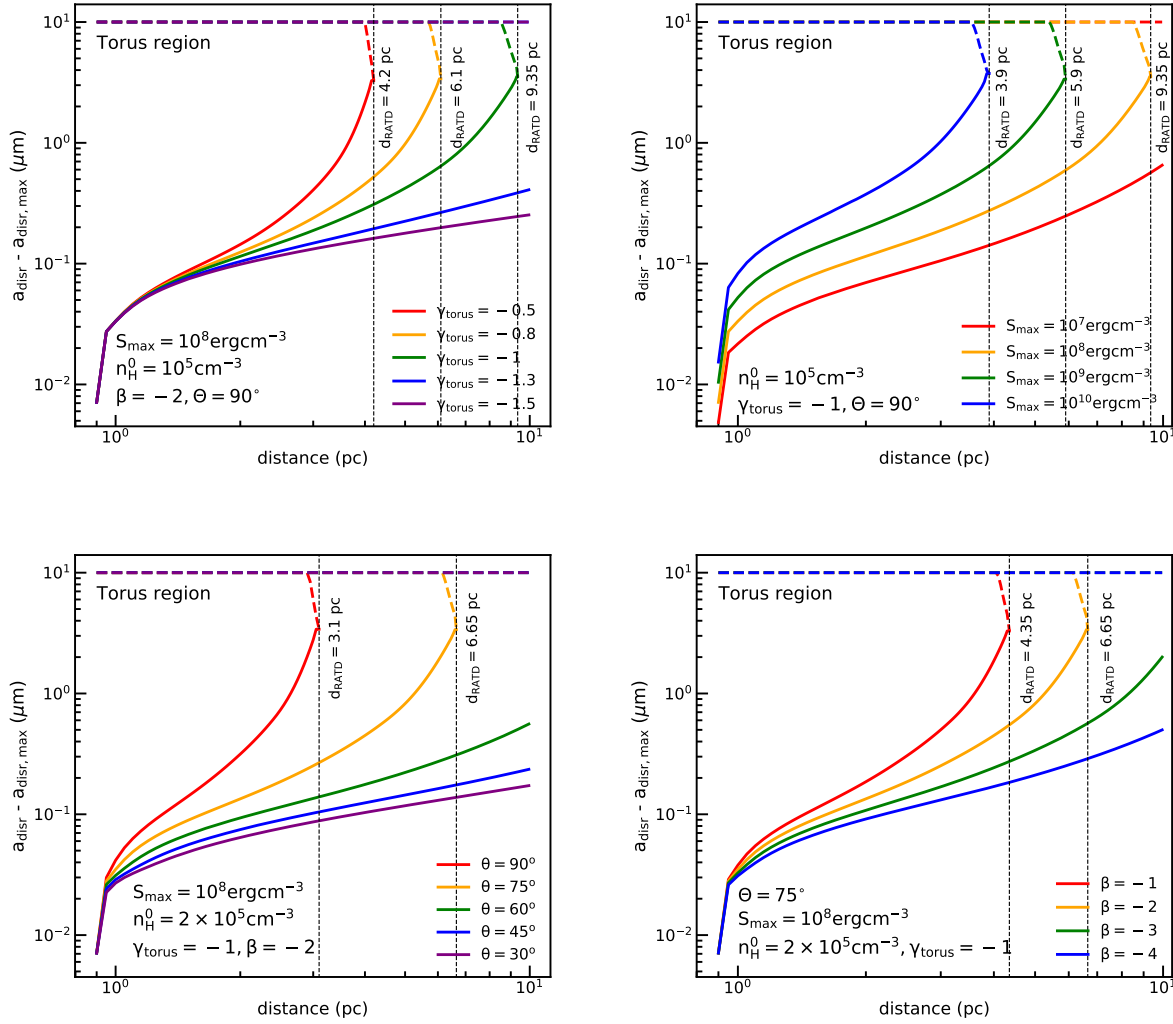


Figure 6. Same as the lower panel of Figure 5 but for different parameters, including the radial power-law index γ_{torus} (upper left panel), the maximum tensile strength S_{max} (upper right panel), the observed angle Θ (lower left panel), and the polar index β (lower right panel). Other parameters of the medium and grains are noted in each panel.

these grains are removed, i.e., the curve at 8 pc, 3 pc, and 2 pc (see the lower panel of Figure 4). NIR-MIR extinction cross section is reduced much stronger than optical range because of the quick removal of micron-sized grains by RATD. In contrast, $\sigma_{\text{ext}}(\lambda)$ at FUV-NUV increases rapidly due to the significant enhancement of small grains in the polar cone. As a consequence, the steepness of FUV-MIR extinction cross section becomes steeper if the cell of grains locates closer to AGN.

In addition, at $d = 100$ pc, 75 pc, and 45 pc, the extinction cross section at $9.7 \mu\text{m}$ produced by the Si-O stretching mode of silicate grains is depleted due to the dominance of large grains in the polar cone. Moving closer to the center of AGN, the extinction at $9.7 \mu\text{m}$ is higher due to the increase of small polar dust.

The right panel of Figure 7 shows similar results as the left one, but for grains with $S_{\text{max}} = 10^9 \text{ erg cm}^{-3}$. The extinction cross section curve will be steeper toward FUV in the active region of RATD. However, the curve produced by grains with $S_{\text{max}} = 10^9 \text{ erg cm}^{-3}$ only shows a significant rise in FUV-NUV range within 8 pc due to the narrower active region of RATD. Further than that, it becomes flattened due to the presence of large grains and ceases when polar dust is not modified by RATD, i.e., the curve at $d = 45$ pc, 75 pc, and 100 pc. Besides, the high extinction at $9.7 \mu\text{m}$ for $S_{\text{max}} = 10^8 \text{ erg cm}^{-3}$ only happens within $d < 25$ pc, which is smaller than $d < 45$ pc in the left panel.

The left panel of Figure 8 shows the final extinction curves, A_λ , produced by grains in the polar re-

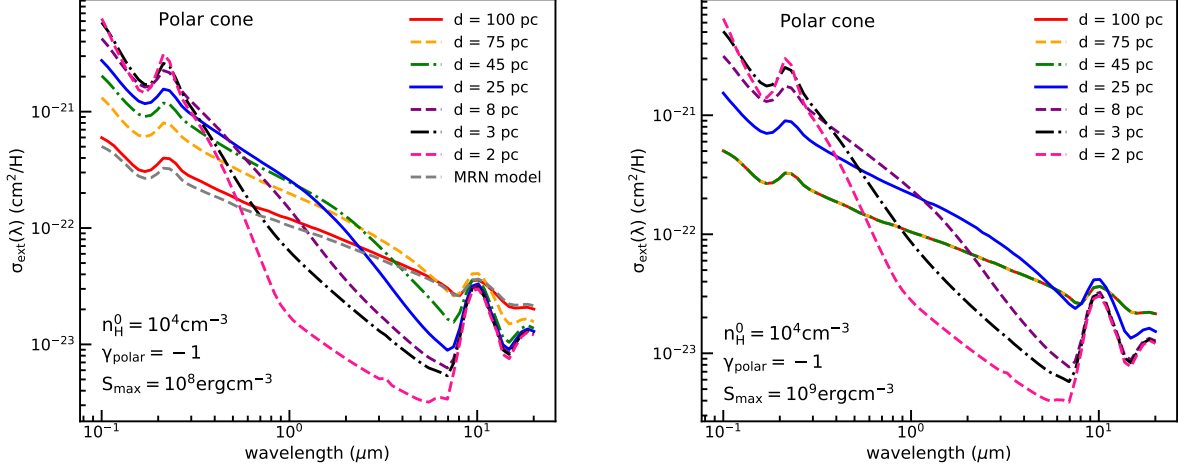


Figure 7. Extinction cross-section per H, $\sigma_{\text{ext}}(\lambda)$, caused by grains in a thin cell located at different distances for $S_{\text{max}} = 10^8 \text{ erg cm}^{-3}$ (left panel) and $S_{\text{max}} = 10^9 \text{ erg cm}^{-3}$ (right panel) for the torus. The gray dashed line in the left panel is produced by original grains that follows the MRN size distribution. As decreasing distances to the center of AGN, FUV-NUV extinction increases while optical-MIR extinction decreases owing to the strong conversion of large grains to smaller sizes by RATD.

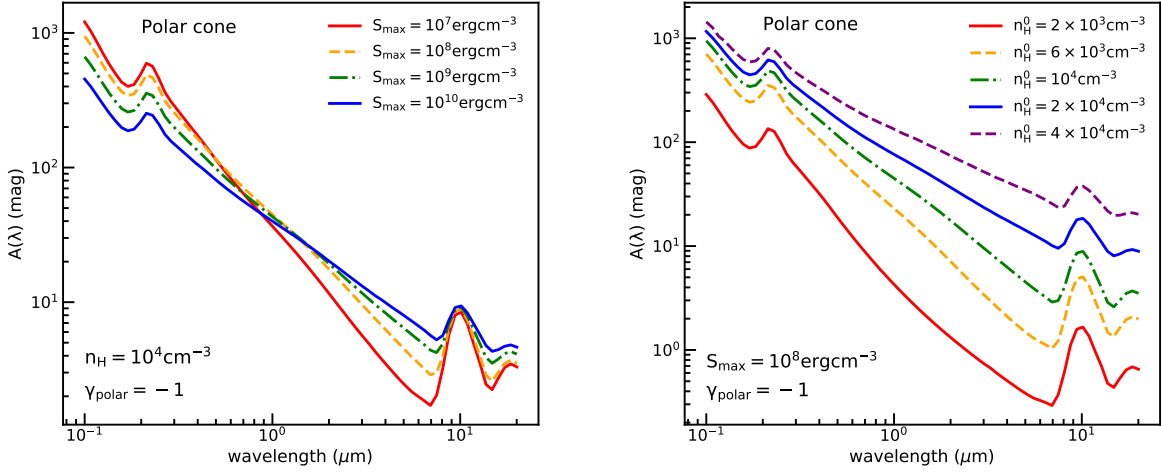


Figure 8. Final extinction curves caused by grains in the polar region within 100 pc for different values of S_{max} , assuming $n_{\text{H}} = 10^4 \text{ cm}^{-3}$ and $\gamma_{\text{polar}} = -1$ (left panel), and for different values of n_{H}^0 , assuming $\gamma_{\text{polar}} = -1$ and $S_{\text{max}} = 10^8 \text{ erg cm}^{-3}$ (right panel).

gion within 100 pc from the sublimation front for different values of S_{max} , assuming $n_{\text{H}}^0 = 10^4 \text{ cm}^{-3}$ and $\gamma_{\text{polar}} = -1$. The extinction curve for high tensile strength of $S_{\text{max}} = 10^{10} \text{ erg cm}^{-3}$ exhibits a prominent rise from MIR to FUV. This slope is produced by the decrease in optical-MIR extinction and the increase in FUV-NUV extinction due to the significant conversion of large polar dust to smaller sizes near the center of AGN (see the lower panel of Figure 4 and Figure 7). Grains with $S_{\text{max}} < 10^{10} \text{ erg cm}^{-3}$ extinct FUV-NUV

stronger but optical-MIR weaker. As a result, the slope of the extinction curve in FUV-MIR range will become steeper toward the blue. The $9.7 \mu\text{m}$ extinction for lower S_{max} is also stronger due to higher abundance of small silicate grains by RATD.

The right panel of Figure 8 shows similar results as the left one, but for different values of the initial gas density, assuming $\gamma_{\text{polar}} = -1$ and $S_{\text{max}} = 10^8 \text{ erg cm}^{-3}$. For a given S_{max} , grains in the polar cone with lower density produce the clear far-UV rise extinction curve and the

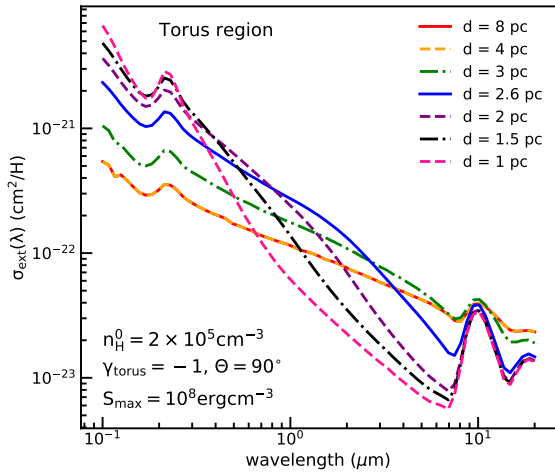


Figure 9. Extinction cross section, $\sigma_{\text{ext}}(\lambda)$, caused by dust in the torus observed along the equatorial plane at different cell distances, assuming $S_{\text{max}} = 10^8 \text{ erg cm}^{-3}$, $n_{\text{H}}^0 = 2 \times 10^5 \text{ cm}^{-3}$, $\gamma_{\text{torus}} = -1$, and $\beta = -2$. The extinction cross-section near AGN shows a steeper rise toward FUV than ones produced by dust at a distant cell.

strong $10 \mu\text{m}$ extinction feature due to the strong enhancement of small grains by RATD. However, its magnitude is smaller than ones produced in higher density polar cone because of the proportional of $A(\lambda)$ and n_{H} (see Equations 20 and 18).

6.1.2. Torus region

Figure 9 shows the extinction cross section, $\sigma_{\text{ext}}(\lambda)$, produced by grains at different distances in the mid-plane of the circumnuclear region, assuming $S_{\text{max}} = 10^8 \text{ erg cm}^{-3}$, $n_{\text{H}}^0 = 10^5 \text{ cm}^{-3}$, $\gamma_{\text{torus}} = -1$, and $\beta = -2$. Similar to Figure 7, the extinction cross section curve will become steeper toward FUV with decreasing distances due to the predominance of small grains by RATD. The $9.7 \mu\text{m}$ absorption feature is also prominent for the cell near the center of AGN.

Figure 10 shows total extinction curves A_{λ} produced by all grains from the sublimation front to the outer region of torus at 10 pc with different values of S_{max} , assuming $n_{\text{H}}^0 = 10^5 \text{ cm}^{-3}$, $\gamma_{\text{torus}} = -1$, and $\beta = -2$. From top to bottom, the observed angle Θ changes from 90° to 75° and 60° , respectively. Similar to the left panel of Figure 8, for a fixed line of sight, as S_{max} decreases, optical-MIR extinction drops while FUV-NUV extinction rises, resulting in the steep far-UV rise extinction curve. The $9.7 \mu\text{m}$ feature is also extinct stronger due to the higher abundance of small grains. By changing the observed angle from the edge-on to the face-on view, the slope of FUV-MIR extinction curves of all consid-

ered cases of S_{max} become steeper toward shorter wavelengths, and the $9.7 \mu\text{m}$ feature becomes stronger. However, its magnitude slightly decreases due to the fast reduction of n_{H} above the equatorial plane.

Figure 11 shows the similar results as Figure 10, but for different values of n_{H}^0 , assuming $S_{\text{max}} = 10^8 \text{ erg cm}^{-3}$. The extinction curve shows a clear rise from MIR to FUV, and the extinction feature at $10 \mu\text{m}$ becomes prominent for the lower gas density. The magnitude of the curve is smaller due to the proportional between $A(\lambda)$ and n_{H} . These features are clearer when one observes AGN at the face-on direction due to the expansion of active region of RATD (see the lower left panel of Figure 6).

In conclusion, the modification of grains around AGN by RATD results in the far-UV rise extinction curve. The slope of the extinction curve depends on the RATD efficiency. Even when RATD is not effective at large distances from AGN, the net observed extinction curve is still steeper than the curve without RATD due to the enhancement of small grains near AGN center.

6.2. Color excess, $E(B - V)$, and total-to-selective extinction ratio, R_V

Using the dust extinction $A(\lambda)$ obtained in Section 6.1, we can calculate the color excess $E(B - V) = A_B - A_V$ with A_B and A_V being the extinction at blue and visible wavelength of $\lambda = 0.45 \mu\text{m}$ and $0.55 \mu\text{m}$, respectively. Then, we can get the total-to-selective visual extinction ratio $R_V = A_V/E(B - V)$.

6.2.1. Polar cone

The upper panel of Figure 12 shows the variation of the color excess over the column density, $E(B - V)_{\text{cell}}/N_{\text{H}}$, for grains in the cell of thickness d_{cell} located at distances d from 2 pc to 100 pc in the polar cone, assuming different values of S_{max} , $n_{\text{H}}^0 = 10^4 \text{ cm}^{-3}$ and $\gamma_{\text{polar}} = -1$. At $d \sim 100 \text{ pc}$, $E(B - V)_{\text{cell}}/N_{\text{H}}$ for $S_{\text{max}} = 10^{10} \text{ erg cm}^{-3}$ is rather low of $\sim 0.25 \times 10^{-22} \text{ mag cm}^2$ due to the presence of large grains beyond the active region of RATD of $d_{\text{RATD}} \geq 17 \text{ pc}$ (see the lower panel of Figure 4). Toward the AGN center, the value of $E(B - V)_{\text{cell}}/N_{\text{H}}$ increases due to the enhancement of small grains by RATD (see Figure 7), then it drops when small grains are further disrupted near the sublimation front (see the lower panel of Figure 4). By decreasing the maximum tensile strength, $E(B - V)_{\text{cell}}/N_{\text{H}}$ starts to rise at larger distances due to larger active region of RATD.

The lower panel of Figure 12 shows similar results as the upper panel, but for $E(B - V)/N_{\text{H}}$ produced by all grains from the sublimation front to distances d . In general, the value of $E(B - V)/N_{\text{H}}$ increases with decreas-

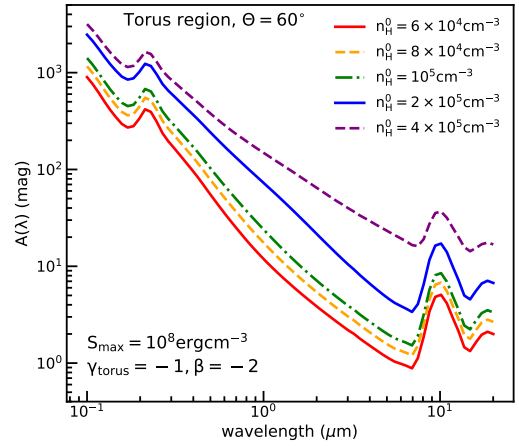
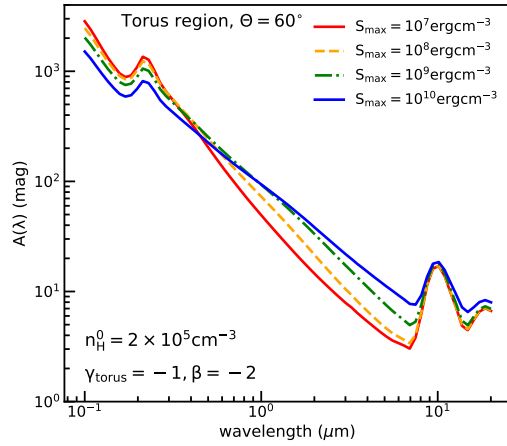
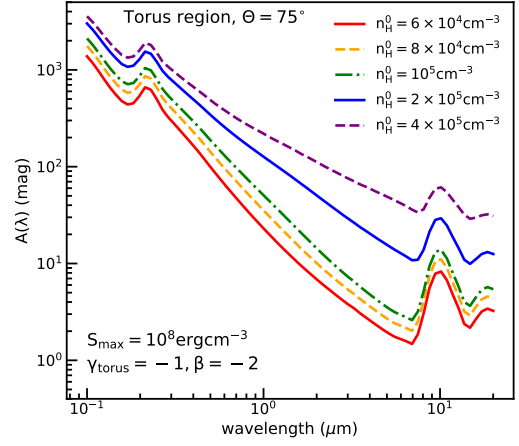
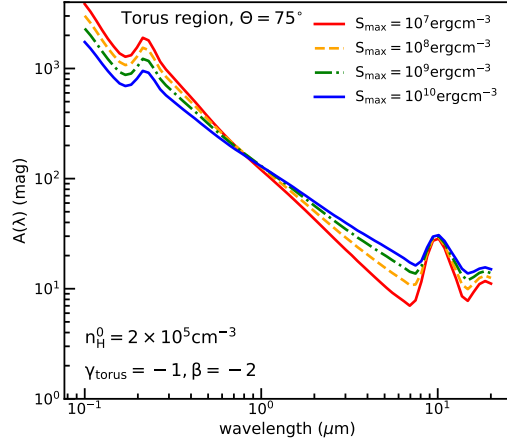
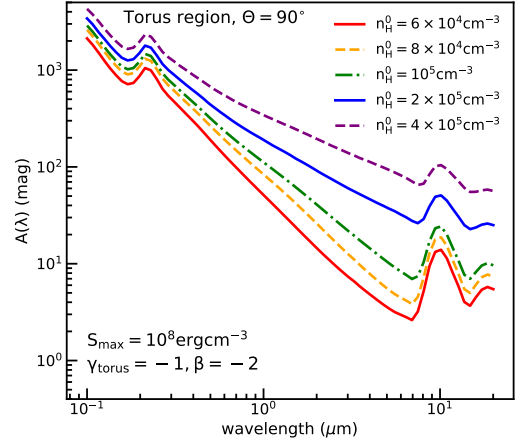
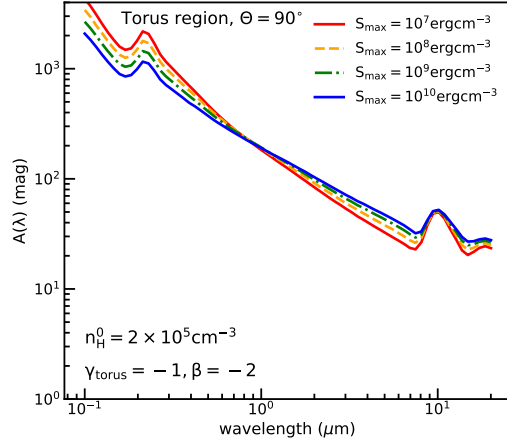


Figure 10. Total extinction curves produced by dust in the torus within 10 pc from the center of AGN for different values of S_{\max} , assuming $n_{\text{H}}^0 = 2 \times 10^5 \text{ cm}^{-3}$, $\gamma_{\text{torus}} = -1$ and $\beta = -2$. From top to bottom, the observed angle changes from $\Theta = 90^\circ$ to $\Theta = 75^\circ$ and 60° , respectively

Figure 11. Same as Figure 10 but for different values of n_{H}^0 , assuming $S_{\max} = 10^8 \text{ erg cm}^{-3}$, $\gamma_{\text{torus}} = -1$, and $\beta = -2$.

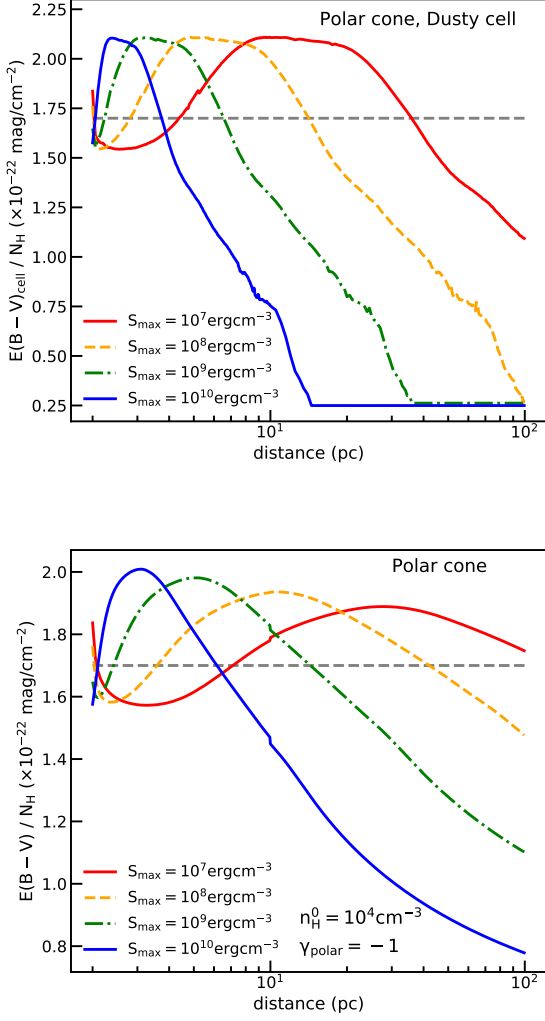


Figure 12. Variation of the color excess per H produced by grains in the cell of thickness d_{cell} , $E(B-V)_{\text{cell}}$ (upper panel) and $E(B-V)$ by all grains from the sublimation front to distance d in the torus (lower panel), assuming different values of S_{max} , $n_{\text{H}}^0 = 10^4 \text{ cm}^{-3}$, and $\gamma_{\text{polar}} = -1$. The horizontal black dashed line is the typical Galactic normalized color excess of $E(B-V)/N_{\text{H}} = 1.7 \times 10^{-22} \text{ mag cm}^{-2}$.

ing distances to the center region due to the increase of small grains by RATD and slightly decreases near the sublimation front when almost such small grains are destroyed. At $d \leq 10 \text{ pc}$, the value of $E(B-V)/N_{\text{G}}$ for lower S_{max} may be larger than the one for higher S_{max} due to the large active region of RATD.

The upper panel of Figure 13 shows the variation of the total-to-selective visual extinction ratio $R_{V\text{cell}}$ due to grains in the cell as a function of distances, assuming the same condition as Figure 12, i.e., different values of S_{max} and $n_{\text{H}}^0 = 10^4 \text{ cm}^{-3}$. At large distances d from the

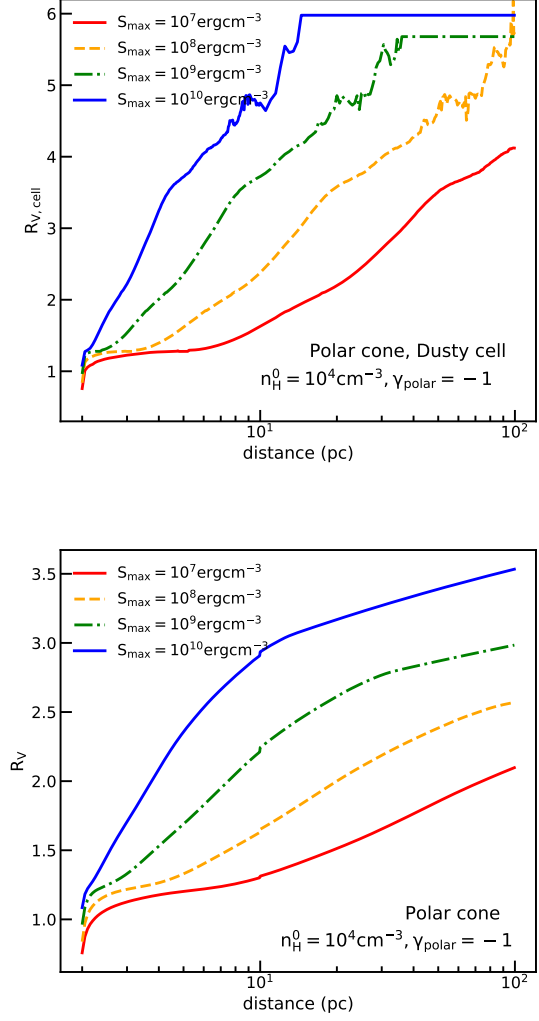


Figure 13. Variation of the total-to-selective visual extinction ratio due to grains in the cell at different distances, $R_{V\text{cell}}$ (upper panel), and R_V due to total grains from the sublimation front to distance d (lower panel), for the torus, assuming different values of S_{max} , $n_{\text{H}}^0 = 10^4 \text{ cm}^{-3}$ and $\gamma_{\text{polar}} = -1$.

center of AGN, the disruption does not occur and $R_{V\text{cell}}$ is flat at $R_{V\text{cell}} \sim 6$. Note that the value $R_{V\text{cell}}$ here exceeds the typical value of 3.1 for the standard ISM because very large grains of $a > 1 \mu\text{m}$ are assumed to exist here. Then, toward the center region, the value of $R_{V\text{cell}}$ decreases continuously from $R_{V\text{cell}} = 6$ to ~ 1 due to increasing disruption of grains by RATD. At the same distance, $R_{V\text{cell}}$ is larger for a higher tensile strength due to weaker RATD.

The lower panel of Figure 13 shows the similar results to the upper panel, but for the variation of R_V produced by all grains contained in the region between

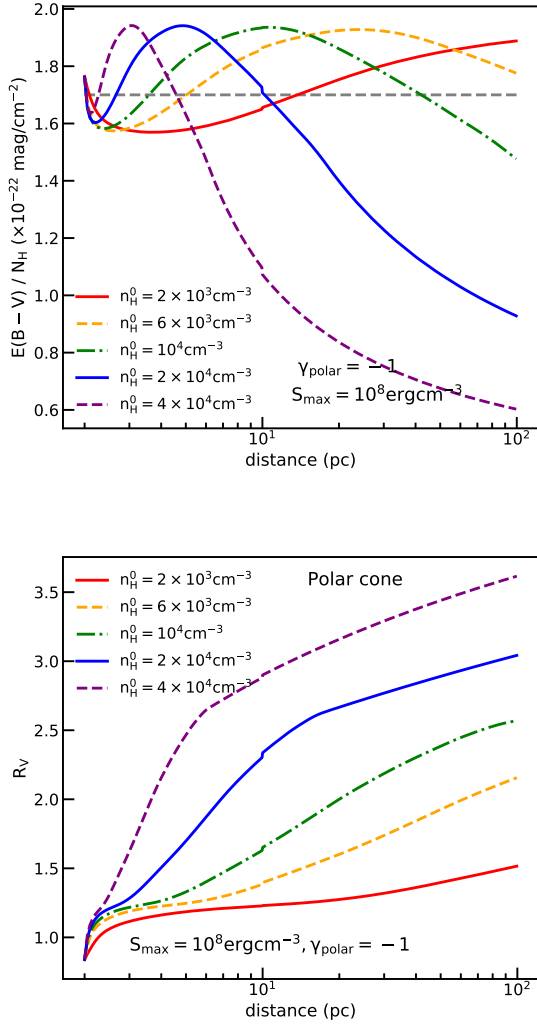


Figure 14. Variation of $E(B-V)/N_H$ and R_V due to all grains from the sublimation front as a function of distances d in the polar cone with different values of n_H^0 , assuming $S_{\max} = 10^8$ erg cm $^{-3}$ and $\gamma_{\text{polar}} = -1$.

the sublimation front and distance d . At $d \sim 100$ pc, with $n_H^0 = 10^4$ cm $^{-3}$, one can see that grains with $S_{\max} \leq 10^8$ erg cm $^{-3}$ produce $R_V \leq 2.5$, much smaller than the Galactic standard value of $R_V = 3.1$. It arises from the significant reduction of the optical-MIR extinction due to the strong removal of large grains by RATD near the center of AGN (see Figures 7 and 8). Thus, the visual extinction A_V in this case is always smaller than $A_{V\text{cell}}$ produced in a cell at the same distance, resulting in a smaller value of R_V . The value of R_V decreases with decreasing d , but at a much smaller rate compared to the upper panel. Besides, at the same cloud distance d , R_V is smaller for the lower maximum tensile strength because of the higher RATD efficiency.

For example, at 100 pc, R_V decreases from ~ 2.5 to ~ 2 if the maximum tensile strength decreases from 10^8 erg cm $^{-3}$ to 10^7 erg cm $^{-3}$. However, in case of compact grains of $S_{\max} \geq 10^9$ erg cm $^{-3}$, the observed value of R_V can increase to ≥ 3 due to the dominance of sub-micron and micron grains in the polar direction, i.e., grains of $a \geq 0.1$ μm start to survive at $d \geq 2$ pc for $S_{\max} \geq 10^9$ erg cm $^{-3}$ (see the lower panel of Figure 4).

The upper panel of Figure 14 shows the variation of $E(B-V)/N_H$ due to grains from the sublimation front to distance d in the polar cone, assuming different gas density profiles and $S_{\max} = 10^8$ erg cm $^{-3}$. For a fixed maximum tensile strength, the normalized color excess $E(B-V)/N_H$ starts to change from the value produced by original dust grains at larger distances for smaller gas density due to the larger active region of RATD. On the other hand, the corresponding total-to-selective visual extinction ratio R_V (lower panel) drops faster with decreasing distances to AGN center and shows smaller values for lower gas density.

6.2.2. Torus region

Figure 15 shows the variation of $E(B-V)_{\text{cell}}/N_H$ (upper panel) and the corresponding $R_{V\text{cell}}$ (lower panel) due to torus dust grains at different cell's distances on the equatorial plane, assuming different values of n_H^0 and $S_{\max} = 10^8$ erg cm $^{-3}$. Similar to the polar cone, the value of $E(B-V)_{\text{cell}}/N_H$ and $R_{V\text{cell}}$ is different from the ones produced by original grains which follow the MRN distribution when RATD starts to modify the grain size distribution. $R_{V\text{cell}}$ decreases with decreasing distances to the center region and exhibits smaller values in lower gas density circumnuclear region. For example, grains in the cell at 10 pc give $R_{V\text{cell}} \sim 5.5, 4$, and 3 if the initial gas density of the torus decreases from $n_H^0 = 10^5$ cm $^{-3}$ to 8×10^4 cm $^{-3}$ and 6×10^4 cm $^{-3}$, respectively.

Figure 16 shows the same results as Figure 15, but due to grains from the sublimation front to distance d . Similar to the results in the lower panel of Figure 14, one can get small values of $R_V \sim 1 - 2.5$ if the torus size is small and the gas density is low. For example, for optically thin torus with $n_H^0 < 2 \times 10^5$ cm $^{-3}$, one can get $R_V \sim 1.8 - 2.5$ with the torus size of radius up to $d \geq 10$ pc. In contrast, with high density of $n_H^0 = 4 \times 10^5$ cm $^{-3}$, one only can get $R_V \leq 3$ if the torus size has the outer boundary at $d \sim 4$ pc. Further than that, R_V quickly rises to $R_V \sim 3.5$ due to the presence of large grains.

Moreover, by changing the observed direction from the edge-on view to the face-on view, the total-to-selective visual extinction ratio produced in the isolated cell $R_{V\text{cell}}$ and in the cloud extending from the sublimation front R_V decreases. It arises from the stronger removal

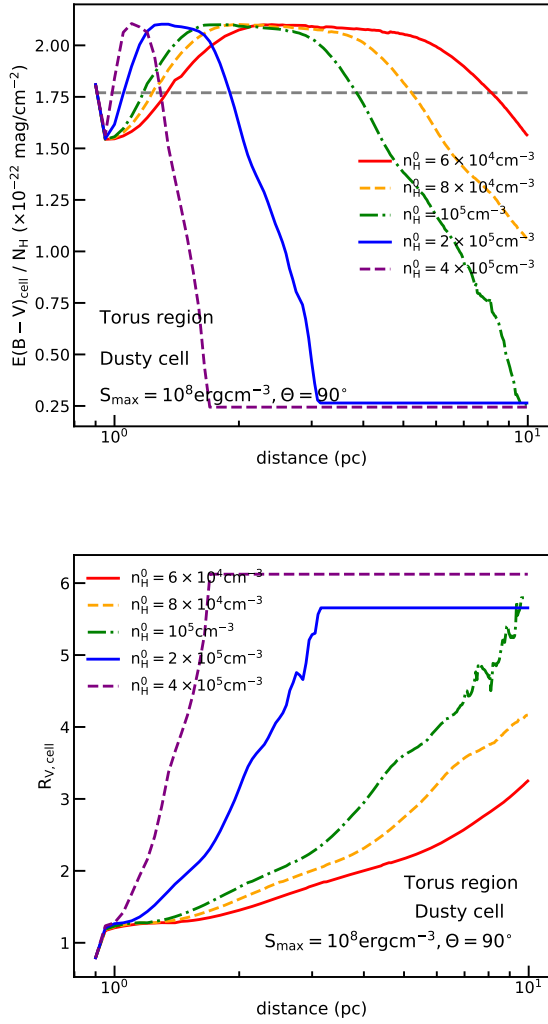


Figure 15. Variation of $E(B - V)_{\text{cell}}/N_{\text{H}}$ (upper panel) and $R_{V,\text{cell}}$ (lower panel) produced by grains in the torus at different cell's distance on the equatorial plane with different values of n_{H}^0 , assuming $S_{\text{max}} = 10^8 \text{ erg cm}^{-3}$, $\gamma_{\text{torus}} = -1$, $\beta = -2$ and $\Theta = 90^\circ$.

of large grains in the region above and below the equatorial plane of AGN by RATD (see the lower left panel of Figure 6). In contrast, the corresponding color excess $E(B - V)_{\text{cell}}/N_{\text{H}}$ and $E(B - V)/N_{\text{H}}$ increase due to the enhancement of small grains by RATD.

7. DISCUSSION

In this section, we discuss the implications of our modeling results for photometric of AGN.

7.1. Photometric observations toward AGN

7.1.1. Extinction curves with a steep far-UV rise

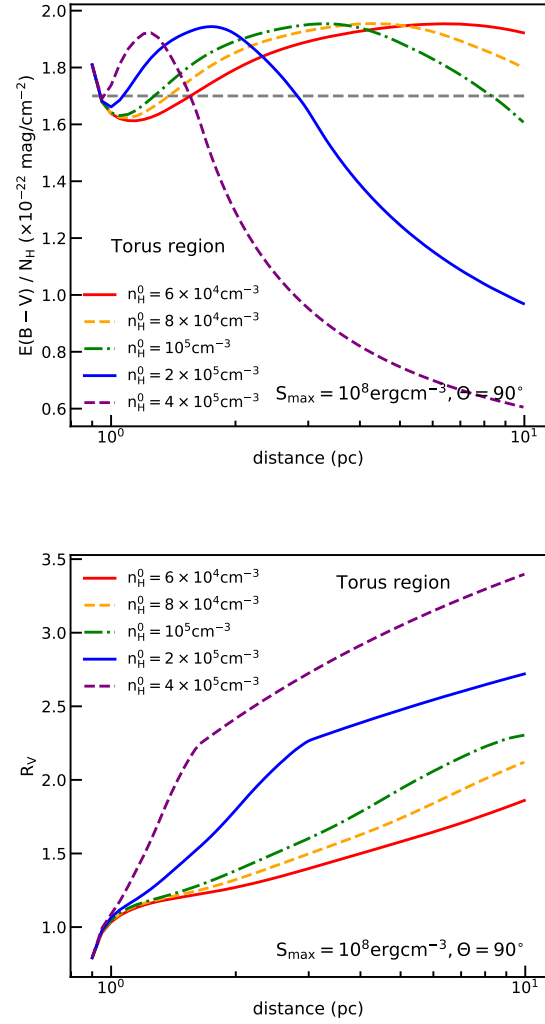


Figure 16. Similar to Figure 14 but for grains within 10 pc in the torus, assuming $S_{\text{max}} = 10^8 \text{ erg cm}^{-3}$, $\gamma_{\text{torus}} = -1$, $\beta = -2$ and $\Theta = 90^\circ$.

Photometric observations toward individual AGN frequently report a 'red tail' in its spectral energy distribution (SED) (Webster et al. 1995, Brotherton et al. 2001, Richards et al. 2002), which is proposed to originate from the intrinsic reddening caused by the central engine and the external dust in the host galaxy. By analyzing the spectra of 4576 quasars from the Sloan Digital Sky Survey (SDSS), Richards et al. (2003) showed that the intrinsic slope of their SED is consistent with its general spectrum. Thus, the 'red tail' in the curves is originated from the extinction of grains in its host galaxy. By fitting the observational data with different dust models, they found that the extinction curves of 273 out of 4576 quasars (6 %) are best described by the SMC-dust model, suggesting the dominance of small

grains of size $a \leq 0.1 \mu\text{m}$ in the host galaxy. Similarly, the study of 9566 quasars from SDSS and expanding to longer wavelengths using a subset of 1866 SDSS-Two Micron All Sky, Hopkins et al. (2004) came to the same conclusion.

In Section 6.1, we show that RATD can convert large grains of $a \geq 0.1 \mu\text{m}$ into small sizes up to 100 pc in the polar cone and 10 pc in the torus region around AGN. Consequently, optical-MIR dust extinction significantly decreases, while FUV-MIR extinction increases, resulting in a steep rise from MIR to far-UV range compared to the standard extinction curve of our galaxy. Thus, the 'SMC'-like extinction curve observed toward many individual AGN can be successfully explained by the effect of RATD on dust in AGN environments.

Indeed, the extinction curves of AGN that show the steep far-UV rise are not completely described by the SMC-like dust model. Instead, its steepness varies between the Milky Way (MW), Large Magellanic Cloud (LMC), and SMC-like extinction curve. In detail, the rise of dust extinction from λ 3500 – 4000 Å to NUV observed toward NGC 3227 by Crenshaw et al. (2001) is higher than the slope of the SMC-like curve. The observed extinction curve of Ark 564 shows a steeper slope than ones induced by interstellar grains, but shallower than the SMC-like curve and does not exhibit the 2175 Å bump (Crenshaw et al. 2002). The well-determined extinction curve of B3 0754 +394 and Ton 951 studied by Gaskell & Benker (2007) can be described by the SMC and LMC-like dust models, respectively. However, the curve of Ton 951 shows a flat in FUV, suggesting the removal of very small grains. The dust reddening of Mrk 304 is also fitted well with LMC-like dust model, but its curve is not-well constrained (Gaskell & Benker 2007).

Theoretically, the different steepness of the FUV-MIR extinction curve implies different grain size distributions. In Section 5, we show that the modification of dust grains around AGN by RATD strongly depends on their internal structure and the properties of AGN environments. In particular, in both the polar cone and torus region (Section 5), we show that large grains are easier to be disrupted to smaller sizes by RATD for lower gas density and lower maximum tensile strength of grains. Consequently, the outcome extinction curves in these cases will present the sharp rise toward far-UV compared with other cases (see Section 6.1). Therefore, RATD appears to be a suitable explanation for the diversity of steepness of extinction curves observed toward many AGN. Moreover, if RATD can reproduce the 'red-ten' AGN, fitting extinction curves produced by RATD with observational data can help us constrain dust properties in AGN environments.

For example, the very steep far-UV rise extinction curve observed toward NGC 3227 (Crenshaw et al. 2001) may arise from the high efficiency of RATD around the nuclei of the host galaxy. It thus implies that grains are likely to have a composite structure (i.e., low S_{max}) instead of a compact one. In contrast, the intermediate slope between LMC and MW-like extinction curve observed toward Ark 564 (Crenshaw et al. 2002), the SMC-like curve, and the LMC-like curve observed toward B3 0754+ 394 and Ton 951 (Gaskell & Benker 2007) suggests a moderate efficiency of RATD.

7.1.2. Low dust reddening of AGN

Several studies of the dust reddening toward AGN report a low value of $E(B-V)/N_{\text{H}}$ and $A_{\text{V}}/N_{\text{H}}$ compared with the typical value in the interstellar medium. For example, most of 19 Seyfert galaxies studied by Maiolino et al. (2001) exhibit a low value of $E(B-V)/N_{\text{H}}$ by a factor of 3-100 compared with the standard value of $1.7 \times 10^{-22} \text{ mag cm}^2$ produced by interstellar dust grains. The low value of $A_{\text{V}}/N_{\text{H}}$ is also revealed through other evidences such as the weak broad line emission at $H\alpha$ and $H\beta$ in intermediate 1.8-1.9 type Seyfert, broad absorption at soft and hard X-ray range in Broad Absorption Line (BAL) QSO (Reichert et al. 1985, Maiolino et al. 2001). This anomalous feature is attributed to the different properties of grains in the AGN environments. For example, Maiolino et al. (2001) suggested that the low value of $E(B-V)/N_{\text{H}}$ may arise from the dominance of large grains of $\geq 0.1 \mu\text{m}$. However, large grains produce a large visual extinction, which is inconsistent with the observed low value of $A_{\text{V}}/N_{\text{H}}$.

In Section 6.1, we show that the RATD effect can reduce the optical to MIR extinction produced by polar and torus dust grains. Thus, by observing AGN in both the edge-on and face-on directions, one can obtain the low value of $A_{\text{V}}/N_{\text{H}}$ that is produced by the strong removal of large grains of $a \geq 0.1 \mu\text{m}$ by RATD in AGN environments.

However, the enhancement of small grains by RATD makes the extinction curve steeper, which increases the color excess $E(B-V)$ compared to the case of no dust disruption. Thus, the ratio $E(B-V)/N_{\text{H}}$ can be higher or lower than the typical Galactic value of $1.7 \times 10^{-22} \text{ mag cm}^2$, depending on the destruction level of RATD in this region. In particular, one can observe the low value of $E(B-V)/N_{\text{H}} \leq 1.7 \times 10^{-22} \text{ mag cm}^2$ if the sub-micron grains responsible for the extinction of optical radiation is less enhanced or totally destroyed by RATD (e.g., see Figure 12 and the upper panel of Figure 14 for polar cone and the upper panel of Figures 15 and 16 for torus region). Therefore, the low value

of $E(B - V)/N_{\text{H}}$ still can be reproduced even if small grains are dominant. The high tensile strength of grains and high density in the surrounding region of AGN may be more preferred.

7.2. Extinction curves without an UV 2175 Å bump

In contrast to the SMC-like extinction curve, several studies based on analyzing the composite spectra quasar and individual AGN by Gaskell et al. (2004) and Gaskell & Benker (2007) report a flat FUV-NUV extinction and a weak 2175 Å bump, that is believed to originate from $\pi - \pi^*$ electronic transition of very small carbonaceous grains (Polycyclic Aromatic Hydrocarbons, PAHs). These features indicate the removal of small grains of $a \leq 0.01 \mu\text{m}$ which are responsible for the FUV-NUV extinction and suggest the preference of large grains of submicron and micron sizes around AGN.

In Section 6.1, we assume that RATD only modifies the grain size, thus, FUV-NUV extinction cannot be reduced due to the enhancement of small grains in both the polar cone and torus region. Now, we consider the destruction mechanisms that can destroy the smallest grains (e.g., sputtering or sublimation). We adopt a space-varying minimum grain size of $a_{\text{min}}(d)$ determined by the Coulomb explosion taken from Tazaki & Ichikawa (2020), which is:

$$a_{\text{min}}(d) = Ad^{\alpha_{\text{amin}}}, \quad (21)$$

where A is the constant at which the minimum grain size at the sublimation front is $a_{\text{min,subli}} = 0.1 \mu\text{m}$, and α_{amin} is the power-law index of the profile.

The upper left panel of Figure 17 shows the variation of the minimum grain size with different power-law indexes α_{amin} from -0.5 to -2 (black line) within 100 pc in the polar cone. The minimum grain size decreases faster with increasing distances if the slope is steeper, i.e., $\alpha_{\text{amin}} = -2$, implying the weak removal of small grains in AGN environment.

The upper right panel shows the final extinction curves produced by the grain size described in the upper left panel with different values of α_{amin} , assuming $S_{\text{max}} = 10^7 \text{ erg cm}^{-3}$ and $n_{\text{H}}^0 = 10^4 \text{ cm}^{-3}$. In the case that small grains of $a \leq 0.05 \mu\text{m}$ are only destroyed within ~ 5 pc from the center region, i.e., $\alpha_{\text{amin}} = -2$, the final extinction curve still shows a steep rise toward FUV. By increasing the value of α_{amin} , small grains are removed to larger distances, resulting in the shallower slope of FUV-NUV extinction curve. For example, the curve will exhibit the flat FUV-NUV extinction if all small grains are removed up to the active of RATD of $d_{\text{RATD}} \sim 50$ pc, i.e., $\alpha_{\text{amin}} = -0.5$.

The lower left and right panels show the same results to the upper right panel, but for grains with $S_{\text{max}} =$

10^9 erg cm^{-3} and $10^{10} \text{ erg cm}^{-3}$, respectively. Similarly, the slope in FUV-NUV extinction becomes shallower if small polar dust of $\leq 0.05 \mu\text{m}$ is totally destroyed in the active region of RATD. The change from steep UV-rise to 'gray' extinction curve is faster for higher tensile strength of grains, and also higher gas density.

In conclusion, the strong removal of small grains of $a < 0.05 \mu\text{m}$ up to the active region of RATD induces the flatten in FUV-NUV extinction and the predominance of large grains as in the conclusion of Gaskell et al. (2004) and Gaskell & Benker (2007).

The destruction of small grains around AGN is first studied by Laor & Draine (1993) for the polar cone and by Barvainis (1987) for the torus region. They found that near the center of AGN, grains are quickly sublimated to the gas phase due to the intense UV-optical radiation. Weingartner et al. (2006) and recently Tazaki et al. (2020) study the effect of Coulomb explosion in AGN environments. They found that small grains are charged in the ionized polar cone then are destroyed up to ~ 10 pc, successfully reproducing the 'gray' extinction curve at this distance. This mechanism does not work well in the torus region due to optically thick environments. However, Coulomb explosion requires X-ray and extreme UV radiation, such as its efficiency is much weaker than RATD that can be effective with longer wavelength photons, i.e., optical-MIR, because such energetic photons are efficiently absorbed. Beside thermal sublimation and Colomb explosion, small grains around AGN also can be destroyed by non-thermal sputtering and MEchanical Torque Disruption (METD) (Hoang & Lee 2020). In the former mechanism, grains are accelerated to hypersonic speeds, i.e., $v \geq 500 \text{ km s}^{-1}$, by the strong radiation pressure from AGN center and be destroyed when moving into the ambient gas. The latter mechanism shares the same principle with RATD. However, in METD, grains are spun up by stochastic mechanical torques induced by grain-grain collision instead of the radiative torque in RATD. We expect that non-thermal sputtering can modify the distribution of small grain size beyond the active region of thermal sublimation or Coulomb explosion. METD can continue to modify it beyond the region where the speed of grains reduces to $v \leq 500 \text{ km s}^{-1}$ (Hoang & Lee 2020). A detailed study of the effect of METD and other dust destruction mechanisms in both the polar cone and torus of AGN is needed to explain the long-term puzzle of the 'flat' and 'SMC-like dust' extinction curve observed toward AGN.

7.3. The depletion at 9.7 μm absorption feature

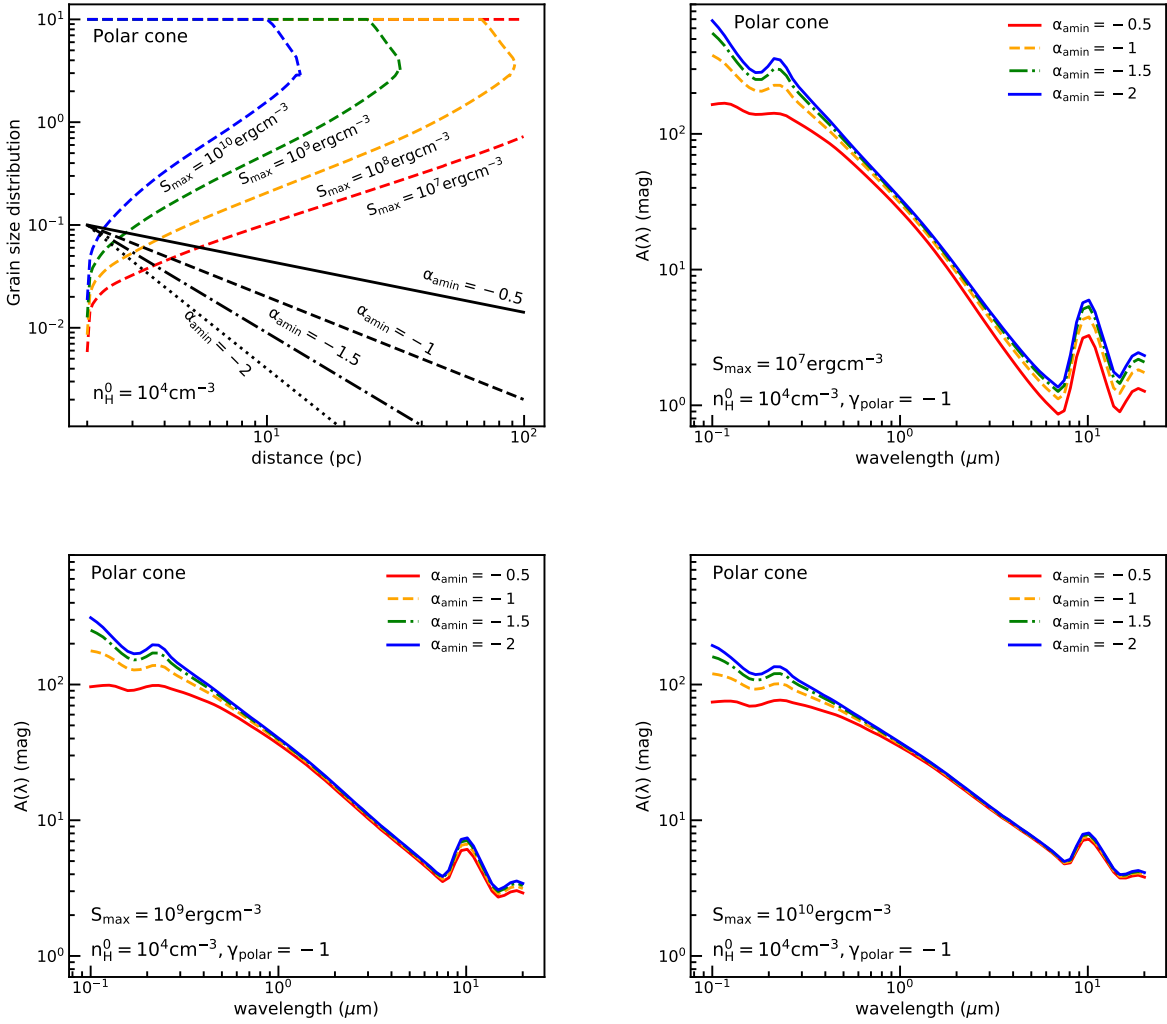


Figure 17. Upper left panel: Variation of minimum grain size with different slope α_{amin} and maximum grain size constrained by RATD with different values of S_{\max} within 100 pc in the polar cone. Other panels: the corresponding final extinction curves of each case.

The absorption/emission at $9.7 \mu\text{m}$ feature produced by the stretching mode of silicate oxide (Si-O) in the observed IR spectrum toward AGN is a tool for studying the properties and composition of grains in AGN environments. Theoretically, the unified model of AGN expects the observed absorption line at $9.7 \mu\text{m}$ in type 2 AGN due to the obscuration of cold dust in the torus. In contrast, one should obtain the emission line in type 1 due to the direct observed view to hot dust near the center of AGN. However, several observations toward type 1 AGN do not show the clear evidence for silicate feature in both absorption and emission (Maiolino et al. 2001, Clavel et al. 2000, Sturm et al. 2005). These anomalous features indicate the difference in physical properties and grain size distribution of grains. In particular, the concentration of silicate grains in clumpy structure

(Rowan-Robinson 1995, Nenkova et al. 2002) or the predominance of micron-sized silicate grains are suggested in order to explain the depletion at $9.7 \mu\text{m}$ absorption in this region (Laor & Draine 1993, Maiolino et al. 2001).

According to Laor & Draine (1993), small grains of $a \leq 0.1 \mu\text{m}$ should be reduced to produce the dominance of large grains in the polar cone of AGN. So is the enhancement of small grains by RATD in conflict with the existence of large grains? The answer is that it depends on AGN environments. In Section 5, we show that large grains of $a \geq 0.1 \mu\text{m}$ in both the polar cone and torus region are only destroyed near the center of AGN for higher gas density and higher internal strength of grains. Consequently, the depletion of $9.7 \mu\text{m}$ silicate absorption feature is still available in spite of accounting for the contribution of RATD in AGN environments (see

Section 6.1). In other words, RATD still supports the depletion of $10\ \mu\text{m}$ in observations. However, if the density around AGN is not dense and grains mostly have composite structure, the strong absorption at $9.7\ \mu\text{m}$ is certainly prominent. The dependence of magnitude of $10\ \mu\text{m}$ with the strength of RATD can be tested with observations using JWST or 10-m class ground-based telescope and be used as a tracer for probing the gas density and characteristic of AGN grains.

On the other hand, in reality, grains may concentrate in dense clumps instead of distributing uniform as our assumption. Depending on the location, the distance to AGN center, and the properties of clumps, grains may be less affected by an intense radiation field of AGN and may survive against RATD. As a result, one would observe the depletion of $9.7\ \mu\text{m}$ feature in the MIR observed spectrum of type 1 AGN. Therefore, the detailed study on the role of RATD with a realistic clumpy distribution model (e.g., Nenkova et al. 2002, Dullemond & van Bemmell 2005, Hönig et al. 2006, Nenkova et al. 2008a, Stalevski et al. 2012, Siebenmorgen et al. 2015) and in polar cone (e.g., Schartmann et al. 2014) is needed to see that if the anomalous feature at $9.7\ \mu\text{m}$ be explained with RATD as in our study.

7.4. Implications for grain structures in the AGN torus

Our obtained results show that grains with a low tensile strength of $S_{\text{max}} \sim 10^7\ \text{erg cm}^{-3}$ can be disrupted to larger distances than those with high tensile strength (see Section 5). From the comparison between our modeling and observational data, one can see the preference of compact grains in both the polar cone and torus region, i.e., higher S_{max} , that is suitable for explaining the observed photometric features of AGN. However, we cannot rule out the presence of large fluffy grains in dense clumps. Moreover, the RATD mechanism implies an increase in the abundance of small grains with decreasing the radial distance to AGN.

8. SUMMARY

We have studied the dust destruction by rotational disruption by RATs in the local environment of AGN and model the extinction curve and other photometric parameters, i.e., R_V , and $E(B - V)$, of AGN. Our main findings are summarized as follows:

1. Large grains of $a \geq 0.1\ \mu\text{m}$ within $\sim 100\ \text{pc}$ in the polar cone and $\sim 10\ \text{pc}$ in the dusty torus can be rotationally disrupted by RATD. The efficiency of RATD increases with increasing radiation field strength of AGN and decreasing the local gas density and the tensile strength of dust grains.

2. Assuming different density profiles and maximum tensile strengths, we calculate the extinction curve produced by polar and grains in the presence of RATD. We find that the final extinction curve produced in both the polar cone and torus region exhibits a steep rise toward far-UV due to the strong disruption of large grains to smaller sizes near the center of AGN. The far-UV rise in extinction is steeper for the lower gas density and lower tensile strength of grains. Thus, the RATD mechanism can explain the 'SMC-like' extinction curve observed toward many individual quasar and AGN.
3. The absence of the $9.7\ \mu\text{m}$ silicate absorption feature can be produced if the RATD effect is not too strong. The dependence of the depth of the $9.7\ \mu\text{m}$ absorption feature with the strength of RATD can be used to probe the physical properties of dust and the effect of radiative feedback of AGN onto the surrounding environment.
4. Combining the RATD mechanism that affects large grains with other destruction mechanisms responsible for destroying very small grains of $\leq 0.05\ \mu\text{m}$ is the key to explain the mixture between the 'gray' and the 'SMC-like' extinction curve observed toward individual AGN. The observed extinction curve will exhibit the flat FUV-NUV extinction if very small grains are strongly depleted up to the active region of RATD.
5. Modeling of the extinction curves for a dusty slab located at different distances d in the polar cone and torus region reveals the strong variation of the curves with d . Both the total-to-selective ratio R_V observed in two regions decreases rapidly with decreasing d . This can be used to interpret observational data for AGN with a clumpy structure where each dusty slab can be considered a clump.

The present paper focuses on grain disruption by RATs and its effect on AGN extinction. It is widely known that RATs can also induce grain alignment with the magnetic field (Lazarian & Hoang 2007, Hoang & Lazarian 2016) that affects the AGN polarization. The optical-UV polarization is dominated by dust/electron scattering (e.g., Marin et al. 2012, Marin 2018a, Marin et al. 2020), while MIR-submillimeter polarization is mainly produced by aligned dust grains (Young et al. 1995, Watanabe et al. 2003, Marin 2018b). The polarized emission from aligned dust grains in IR wavelengths thus becomes a powerful tool for studying magnetic fields in AGN environments (Lopez-Rodriguez et al.

2018a, Lopez-Rodriguez et al. 2020a, Lopez-Rodriguez et al. 2020b). This important issue will be studied in detail in our followup paper.

ACKNOWLEDGMENTS

We are grateful to the referee for helpful comments that improve our manuscript. We thank Le Ngoc Tram for detailed comments on the early period of the draft. T.H. acknowledges the support by the National Research Foundation of Korea (NRF) grants funded by the Korea government (MSIT) through the Mid-career Research Program (2019R1A2C1087045).

REFERENCES

- Antonucci, R. 1993, *ARA& A*, 31, 473, doi: [10.1146/annurev.aa.31.090193.002353](https://doi.org/10.1146/annurev.aa.31.090193.002353)
- Asmus, D., Hönig, S. F., & Gandhi, P. 2016, *ApJ*, 822, 109, doi: [10.3847/0004-637X/822/2/109](https://doi.org/10.3847/0004-637X/822/2/109)
- Asmus, D., Hönig, S. F., Gandhi, P., Smette, A., & Duschl, W. J. 2014, *MNRAS*, 439, 1648, doi: [10.1093/mnras/stu041](https://doi.org/10.1093/mnras/stu041)
- Barvainis, R. 1987, *ApJ*, 320, 537, doi: [10.1086/165571](https://doi.org/10.1086/165571)
- Brotherton, M. S., Tran, H. D., Becker, R. H., et al. 2001, *ApJ*, 546, 775, doi: [10.1086/318309](https://doi.org/10.1086/318309)
- Burke, J. R., & Silk, J. 1974, *ApJ*, 190, 1, doi: [10.1086/152840](https://doi.org/10.1086/152840)
- Clavel, J., Schulz, B., Altieri, B., et al. 2000, *A&A*, 357, 839. <https://arxiv.org/abs/astro-ph/0003298>
- Crenshaw, D. M., Kraemer, S. B., Bruhweiler, F. C., & Ruiz, J. R. 2001, *ApJ*, 555, 633, doi: [10.1086/321522](https://doi.org/10.1086/321522)
- Crenshaw, D. M., Kraemer, S. B., Turner, T. J., et al. 2002, *ApJ*, 566, 187, doi: [10.1086/338058](https://doi.org/10.1086/338058)
- Draine, B. T. 2011, *Physics of the Interstellar and Intergalactic Medium*
- Draine, B. T., Draine, B. T., Flatau, P. J., & Flatau, P. J. 1994, *Journal of the Optical Society of America A: Optics and Image Science (ISSN 0740-3232)*, 11, 1491
- Draine, B. T., & Lee, H. M. 1984, *ApJ*, 285, 89, doi: [10.1086/162480](https://doi.org/10.1086/162480)
- Draine, B. T., & Li, A. 2007, *ApJ*, 657, 810, doi: [10.1086/511055](https://doi.org/10.1086/511055)
- Draine, B. T., & Salpeter, E. E. 1979, *ApJ*, 231, 77, doi: [10.1086/157165](https://doi.org/10.1086/157165)
- Draine, B. T., & Weingartner, J. C. 1996, *ApJ*, 470, 551, doi: [10.1086/177887](https://doi.org/10.1086/177887)
- Dullemond, C. P., & van Bemmell, I. M. 2005, *A&A*, 436, 47, doi: [10.1051/0004-6361:20041763](https://doi.org/10.1051/0004-6361:20041763)
- Efstathiou, A., & Rowan-Robinson, M. 1995, *MNRAS*, 273, 649, doi: [10.1093/mnras/273.3.649](https://doi.org/10.1093/mnras/273.3.649)
- Fritz, J., Franceschini, A., & Hatziminaoglou, E. 2006, *MNRAS*, 366, 767, doi: [10.1111/j.1365-2966.2006.09866.x](https://doi.org/10.1111/j.1365-2966.2006.09866.x)
- Gaskell, C. M., & Benker, A. J. 2007, arXiv e-prints, arXiv:0711.1013. <https://arxiv.org/abs/0711.1013>
- Gaskell, C. M., Goosmann, R. W., Antonucci, R. R. J., & Whysong, D. H. 2004, *ApJ*, 616, 147, doi: [10.1086/423885](https://doi.org/10.1086/423885)
- Giang, N. C., Hoang, T., & Tram, L. N. 2020, *ApJ*, 888, 93, doi: [10.3847/1538-4357/ab5d37](https://doi.org/10.3847/1538-4357/ab5d37)
- Granato, G. L., & Danese, L. 1994, *MNRAS*, 268, 235, doi: [10.1093/mnras/268.1.235](https://doi.org/10.1093/mnras/268.1.235)
- Granato, G. L., Danese, L., & Franceschini, A. 1997, *ApJ*, 486, 147, doi: [10.1086/304502](https://doi.org/10.1086/304502)
- Hoang, T. 2019, *ApJ*, 876, 13, doi: [10.3847/1538-4357/ab1075](https://doi.org/10.3847/1538-4357/ab1075)
- Hoang, T. 2020, *Galaxies*, 8, 52, doi: [10.3390/galaxies8030052](https://doi.org/10.3390/galaxies8030052)
- Hoang, T., Giang, N. C., & Tram, L. N. 2020, *ApJ*, 895, 16, doi: [10.3847/1538-4357/ab8ae1](https://doi.org/10.3847/1538-4357/ab8ae1)
- Hoang, T., & Lazarian, A. 2008, *MNRAS*, 388, 117, doi: [10.1111/j.1365-2966.2008.13249.x](https://doi.org/10.1111/j.1365-2966.2008.13249.x)
- . 2009, *ApJ*, 697, 1316, doi: [10.1088/0004-637X/697/2/1316](https://doi.org/10.1088/0004-637X/697/2/1316)
- . 2014, *MNRAS*, 438, 680, doi: [10.1093/mnras/stt2240](https://doi.org/10.1093/mnras/stt2240)
- Hoang, T., & Lazarian, A. 2016, *ApJ*, 831, 159, doi: [10.3847/0004-637x/831/2/159](https://doi.org/10.3847/0004-637x/831/2/159)
- Hoang, T., Lazarian, A., & Martin, P. G. 2013, *ApJ*, 779, 152, doi: [10.1088/0004-637X/779/2/152](https://doi.org/10.1088/0004-637X/779/2/152)
- Hoang, T., & Lee, H. 2020, *ApJ*, 896, 144, doi: [10.3847/1538-4357/ab9609](https://doi.org/10.3847/1538-4357/ab9609)
- Hoang, T., Tram, L. N., Lee, H., & Ahn, S.-H. 2019, *Nature*, 3, 766–775, doi: [10.1038/s41550-019-0763-6](https://doi.org/10.1038/s41550-019-0763-6)

- Hoang, T., Tram, L. N., Lee, H., Diep, P. N., & Ngoc, N. B. 2021, *ApJ*, 908, 218, doi: [10.3847/1538-4357/abd54f](https://doi.org/10.3847/1538-4357/abd54f)
- Hönig, S. F., Beckert, T., Ohnaka, K., & Weigelt, G. 2006, *A&A*, 452, 459, doi: [10.1051/0004-6361:20054622](https://doi.org/10.1051/0004-6361:20054622)
- Hönig, S. F., & Kishimoto, M. 2010, *A&A*, 523, A27, doi: [10.1051/0004-6361/200912676](https://doi.org/10.1051/0004-6361/200912676)
- Hönig, S. F., Kishimoto, M., Tristram, K. R. W., et al. 2013, *ApJ*, 771, 87, doi: [10.1088/0004-637X/771/2/87](https://doi.org/10.1088/0004-637X/771/2/87)
- Hopkins, P. F., Strauss, M. A., Hall, P. B., et al. 2004, *ApJ*, 128, 1112, doi: [10.1086/423291](https://doi.org/10.1086/423291)
- Hönig, S. F., Kishimoto, M., Antonucci, R., et al. 2012, *ApJ*, 755, 149, doi: [10.1088/0004-637x/755/2/149](https://doi.org/10.1088/0004-637x/755/2/149)
- Krolik, J. H., & Begelman, M. C. 1988, *ApJ*, 329, 702, doi: [10.1086/166414](https://doi.org/10.1086/166414)
- Laor, A., & Draine, B. T. 1993, *ApJ*, 402, 441, doi: [10.1086/172149](https://doi.org/10.1086/172149)
- Lazarian, A., & Hoang, T. 2007, *MNRAS*, 378, 910, doi: [10.1111/j.1365-2966.2007.11817.x](https://doi.org/10.1111/j.1365-2966.2007.11817.x)
- Li, A., & Draine, B. T. 2001, *ApJ*, 554, 778–802, doi: [10.1086/323147](https://doi.org/10.1086/323147)
- López-Gonzaga, N., Burtscher, L., Tristram, K. R. W., Meisenheimer, K., & Schartmann, M. 2016, *A&A*, 591, A47, doi: [10.1051/0004-6361/201527590](https://doi.org/10.1051/0004-6361/201527590)
- Lopez-Rodriguez, E., Antonucci, R., Chary, R.-R., & Kishimoto, M. 2018a, *ApJL*, 861, 0
- Lopez-Rodriguez, E., Dowell, C. D., Jones, T. J., et al. 2020a, *ApJ*, 888, 66, doi: [10.3847/1538-4357/ab5849](https://doi.org/10.3847/1538-4357/ab5849)
- Lopez-Rodriguez, E., Alonso-Herrero, A., García-Burillo, S., et al. 2020b, *ApJ*, 893, 33, doi: [10.3847/1538-4357/ab8013](https://doi.org/10.3847/1538-4357/ab8013)
- Lyu, J., & Rieke, G. H. 2018, *ApJ*, 866, 92, doi: [10.3847/1538-4357/aae075](https://doi.org/10.3847/1538-4357/aae075)
- Maiolino, R., Marconi, A., Salvati, M., et al. 2001, *A&A*, 365, 28, doi: [10.1051/0004-6361:20000177](https://doi.org/10.1051/0004-6361:20000177)
- Manske, V., Henning, T., & Men'shchikov, A. B. 1998, *A&A*, 331, 52
- Marin, F. 2018a, *A&A*, 615, A171, doi: [10.1051/0004-6361/201833225](https://doi.org/10.1051/0004-6361/201833225)
- . 2018b, *MNRAS*, 479, 3142, doi: [10.1093/mnras/sty1566](https://doi.org/10.1093/mnras/sty1566)
- Marin, F., Goosmann, R. W., Gaskell, C. M., Porquet, D., & Dovčiak, M. 2012, *A&A*, 548, A121, doi: [10.1051/0004-6361/201219751](https://doi.org/10.1051/0004-6361/201219751)
- Marin, F., Le Cam, J., Lopez-Rodriguez, E., et al. 2020, *MNRAS*, 496, 215, doi: [10.1093/mnras/staa1533](https://doi.org/10.1093/mnras/staa1533)
- Mathis, J. S., Mezger, P. G., & Panagia, N. 1983, *A&A*, 500, 259
- Mathis, J. S., Rumpl, W., & Nordsieck, K. H. 1977, *ApJ*, 217, 425, doi: [10.1086/155591](https://doi.org/10.1086/155591)
- Nenkova, M., Ivezić, Ž., & Elitzur, M. 2002, *ApJL*, 570, L9, doi: [10.1086/340857](https://doi.org/10.1086/340857)
- Nenkova, M., Sirocky, M. M., Ivezić, Ž., & Elitzur, M. 2008a, *ApJ*, 685, 147, doi: [10.1086/590482](https://doi.org/10.1086/590482)
- Nenkova, M., Sirocky, M. M., Nikutta, R., Ivezić, Ž., & Elitzur, M. 2008b, *ApJ*, 685, 160, doi: [10.1086/590483](https://doi.org/10.1086/590483)
- Rees, M. J., Silk, J. I., Werner, M. W., & Wickramasinghe, N. C. 1969, *Nature*, 223, 788, doi: [10.1038/223788a0](https://doi.org/10.1038/223788a0)
- Reichert, G. A., Mushotzky, R. F., Petre, R., & Holt, S. S. 1985, *ApJ*, 296, 69, doi: [10.1086/163421](https://doi.org/10.1086/163421)
- Richards, G. T., Fan, X., Newberg, H. J., et al. 2002, *ApJ*, 123, 2945, doi: [10.1086/340187](https://doi.org/10.1086/340187)
- Richards, G. T., Hall, P. B., Vand en Berk, D. E., et al. 2003, *ApJ*, 126, 1131, doi: [10.1086/377014](https://doi.org/10.1086/377014)
- Rowan-Robinson, M. 1995, *MNRAS*, 272, 737, doi: [10.1093/mnras/272.4.737](https://doi.org/10.1093/mnras/272.4.737)
- Sazonov, S. Y., Ostriker, J. P., Ciotti, L., & Sunyaev, R. A. 2005, *MNRAS*, 358, 168, doi: [10.1111/j.1365-2966.2005.08763.x](https://doi.org/10.1111/j.1365-2966.2005.08763.x)
- Schartmann, M., Wada, K., Prieto, M. A., Burkert, A., & Tristram, K. R. W. 2014, *MNRAS*, 445, 3878, doi: [10.1093/mnras/stu2020](https://doi.org/10.1093/mnras/stu2020)
- Siebenmorgen, R., Heymann, F., & Efstathiou, A. 2015, *A&A*, 583, A120, doi: [10.1051/0004-6361/201526034](https://doi.org/10.1051/0004-6361/201526034)
- Stalevski, M., Fritz, J., Baes, M., Nakos, T., & Popović, L. Č. 2012, *MNRAS*, 420, 2756, doi: [10.1111/j.1365-2966.2011.19775.x](https://doi.org/10.1111/j.1365-2966.2011.19775.x)
- Sturm, E., Schweitzer, M., Lutz, D., et al. 2005, *ApJ*, 629, L21, doi: [10.1086/444359](https://doi.org/10.1086/444359)
- Tazaki, R., & Ichikawa, K. 2020, *ApJ*, 892, 149, doi: [10.3847/1538-4357/ab72f6](https://doi.org/10.3847/1538-4357/ab72f6)
- Tazaki, R., Ichikawa, K., & Kokubo, M. 2020, arXiv e-prints, arXiv:2002.08023, <https://arxiv.org/abs/2002.08023>
- Tristram, K. R. W., Burtscher, L., Jaffe, W., et al. 2014, *A&A*, 563, A82, doi: [10.1051/0004-6361/201322698](https://doi.org/10.1051/0004-6361/201322698)
- Tristram, K. R. W., Meisenheimer, K., Jaffe, W., et al. 2007, *A&A*, 474, 837, doi: [10.1051/0004-6361:20078369](https://doi.org/10.1051/0004-6361:20078369)
- Tung, N.-D., & Hoang, T. 2020, *ApJ*, 901, 6, doi: [10.3847/1538-4357/abacbf](https://doi.org/10.3847/1538-4357/abacbf)
- Urry, C. M., & Padovani, P. 1995, *PASP*, 107, 803, doi: [10.1086/133630](https://doi.org/10.1086/133630)
- Watanabe, M., Nagata, T., Sato, S., Nakaya, H., & Hough, J. H. 2003, *ApJ*, 591, 714, doi: [10.1086/375514](https://doi.org/10.1086/375514)
- Webster, R. L., Francis, P. J., Petersont, B. A., Drinkwater, M. J., & Masci, F. J. 1995, *Nature*, 375, 469, doi: [10.1038/375469a0](https://doi.org/10.1038/375469a0)
- Weingartner, J. C., & Draine, B. T. 2001, *ApJ*, 548, 296, doi: [10.1086/318651](https://doi.org/10.1086/318651)
- Weingartner, J. C., Draine, B. T., & Barr, D. K. 2006, *ApJ*, 645, 1188, doi: [10.1086/504420](https://doi.org/10.1086/504420)

Young, S., Hough, J. H., Axon, D. J., Bailey, J. A., &
Ward, M. J. 1995, MNRAS, 272, 513,

doi: [10.1093/mnras/272.3.513](https://doi.org/10.1093/mnras/272.3.513)

Yu. Sazonov, S., Ostriker, J. P., & Sunyaev, R. A. 2004,

MNRAS, 347, 144, doi: [10.1111/j.1365-2966.2004.07184.x](https://doi.org/10.1111/j.1365-2966.2004.07184.x)